Time scale disparity yielding acoustic nonreciprocity in a two-dimensional granular-elastic solid interface with asymmetry

Chongan Wang ⓘ,* Sameh Tawfick, and Alexander F. Vakakis ⓘ

Department of Mechanical Science and Engineering, University of Illinois at Urbana-Champaign, Urbana, Illinois 61801, USA

We study nonreciprocal wave transmission across the interface of two dissimilar granular media separated by an elastic solid medium. Specifically, a left, larger-scale and a right smaller-scale granular media composed of two-dimensional, initially uncompressed hexagonally packed granules are interfacing with an intermediate linearly elastic solid, modeled either as a thin elastic plate or a linear Euler-Bernoulli beam. The granular media are modeled by discrete elements and the elastic solid by finite elements assuming a plane stress approximation for the thin plate. Accounting for the combined effects of Hertzian, frictional and rotational interactions in the granular media, as well as the highly discontinuous interfacial effects between the (discrete) granular media and the (continuous) intermediate elastic solid, the nonlinear acoustics of the integrated system is computationally studied subject to a half-sine shock excitation applied to a boundary granule of either the left or right granular medium. The highly discontinuous and nonlinear interaction forces coupling the granular media to the elastic solid are accurately computed through an algorithm with interrelated iteration and interpolation at successive adaptive time steps. Numerical convergence is ensured by monitoring the (linearized) eigenvalues of a nonlinear map of interface forces at each (variable) time step. Due to the strong nonlinearity and hierarchical asymmetry of the left and right granular media, time scale disparity occurs in the response of the interface which breaks acoustic reciprocity. Specifically, depending on the location and intensity of the applied shock, propagating wavefronts are excited in the granular media, which, in turn, excite either (slow) low-frequency vibrations or (fast) high-frequency acoustics in the intermediate elastic medium. This scale disparity is due to the size disparity of the left and right granular media, which yields drastically different wave speeds in the resulting propagating wavefronts. As a result, the continuum part of the interface responds with either low-frequency vibrations—when the shock is applied to the larger-scale granular medium, or high-frequency waves—when the shock is applied to the smaller-scale granular medium. This provides the fundamental mechanism for breaking reciprocity in the interface. The nonreciprocal interfacial acoustics studied here apply to a broad class of asymmetric hybrid (discrete-continuum) nonlinear systems and can inform predictive designs of highly effective granular shock protectors or granular acoustic diodes.

I. INTRODUCTION

Wave propagation in granular media composed of ordered discrete elastic particles (granules) attracts considerable attention from the view of theoretical and experimental nonlinear acoustics. Nesterenko pioneered the field of wave propagation in one-dimensional (1D) homogeneous granular chains composed of initially uncompressed, ordered, linearly elastic, and identical spherical granules interacting in Hertzian contact. Analytical, numerical, and experimental studies validated the transmission of spatially localized, shape-preserving and strongly nonlinear solitary waves—termed Nesterenko solitary waves in these 1D media [1–4]. Due to the nonlinear nature of the Hertzian interactions, the wave speed of a Nesterenko solitary wave is highly dependent on its amplitude [4,5]. Moreover, since the linearized stiffness of the Hertzian granular interactions is zero (in the absence of precompression), the governing acoustics is essentially nonlinear

(i.e., they do not admit linearization even in the limit of small amplitudes), and the speed of sound as defined in classical linear acoustics is zero in these media; hence their designation as "sonic vacua" [1–4]. Also, the strong tunability with energy of the nonlinear acoustics enables interesting and unique features, including frequency pass and stop bands tunable with energy [6], countable infinities of families of standing and traveling nonlinear waves [7,8], and intense nonlinear exchanges [9], targeted energy transfers [10], and break of reciprocity [11–13] in coupled granular chains. These unique acoustic features pave the way for novel acoustic devices and acoustic metamaterials, e.g., acoustic lenses [14,15], shock- and energy-absorbing granular layers [16–18], passive acoustic filters [19], and acoustic switches [20].

Layers of granular materials separated by continuous elastic sheets are commonly used in shock absorption applications including civil engineering constructions. In particular, the layered morphology is ubiquitously used in building retaining walls reinforced by geogrid fabrics [21,22]. In this configuration, alternating layers of soils and elastic fabrics—called geofabrics—are used to reinforce constructions and stabilize

---

*Corresponding author: chongan2@illinois.edu

044906-1

them against dynamic loads, providing a much higher resilience in comparison with unconstrained homogeneous soils. Similar concepts of layered materials are being evaluated for shock absorption outside the civil engineering domains. Hence, in order to better utilize the unique performance of granular media layered with elastic sheets, a natural next step is to further investigate nonlinear wave scattering between these highly discontinuous discrete media and elastic continua, i.e., studying granular-elastic solid interfaces. This requires the study the ordered granular media with nonstandard flexible boundary conditions. Potekin *et al.* [23] first developed an algorithm to study wave scattering at the interface of a 1D granular chain with a linearly elastic cord (tensioned wire), which incorporated interrelated iterations and interpolations at successive time steps. Zhang *et al.* [24] extended that algorithm to study nonlinear wave scattering at the interface of a 1D granular chain with a linear membrane. Both works showed that the energy transmitted to the elastic media were highly discontinuous and dependent on the local impedance mismatch at the interface.

The exploration of nonlinear wave propagation in two-dimensional (2D) and three-dimensional (3D) ordered granular media is still limited. In addition to compressive (normal) Hertzian granular interactions, tangential frictional forces due to rotational effects are unavoidable in higher dimensions. In fact, as shown by Yang and Sutton [25] the omission of frictional interactions due to granular rotations may lead to significant errors when modeling hexagonally packed granular networks. Moreover, Goldenberg and Goldhirsch [26], Chattoraj *et al.* [27], and Charan *et al.* [28] showed that the frictional force may lead to dynamical instabilities. Hence, accounting for these effects may significantly improve the agreement between numerical simulations and experiments [12,26]. By incorporating the combined effects of friction and the flexible boundaries, Wang *et al.* [29] extended the algorithm developed by Potekin *et al.* [23] and Zhang *et al.* [24] to 2D granular-solid interfaces consisting of closely packed, hexagonally ordered granules in contact with thin plates. To avoid numerical instabilities due to frictional effects, a smooth approximation was considered instead of the discontinuous Coulomb friction forces, and a convergence criterion based on the eigenvalues of a linearized iterative map of the granule-plate interaction forces at each time step was formulated to ensure the stability and robustness of the algorithm [27]. That work paved the way for investigating the nonlinear acoustics of 2D nonlinear wave propagation across the interfaces between nonlinear discrete granular media and linearly elastic continua.

Apart from other nonlinear acoustic features, in this work we consider the break of reciprocity in the 2D granular-elastic solid interfaces. Acoustic reciprocity is a fundamental property of linear time invariant systems [30] governed by Sturm-Liouville operators. Basic ways of breaking the reciprocity involve adding odd-symmetric external biases [31–33], inducing time variant properties [34] or imposing nonlinearities in conjunction with some sort of system asymmetry. Given the asymmetry and strong nonlinearity of the considered interfaces it is anticipated that they will possess nonreciprocal acoustics. Previous work mainly focused on the nonreciprocal acoustics of 1D granular systems [11–13],
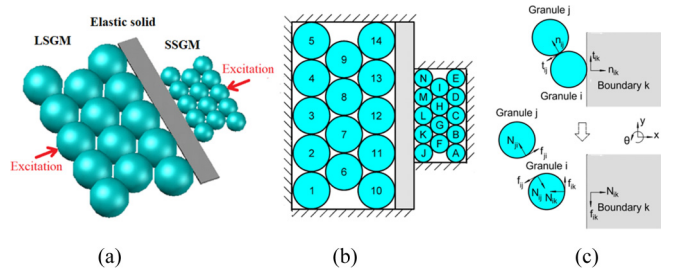

FIG. 1. Schematics of the granular-elastic solid interface subject to shock excitation: (a) 3D isometric view, (b) 2D planar model with boundary conditions, (c) granule-granule and granule-elastic solid contact points, corresponding free body diagrams and notations for normal and tangential interaction forces.

and in acoustical systems with nonlinearity, asymmetry, and internal hierarchy [35–37]. In this work, we will numerically study the break of acoustic reciprocity by applying the same shock excitation to the free boundary of the left (larger scale) and then of the right (smaller scale) granular medium and compare the responses at the corresponding excitation positions. We will investigate how wave transmission in the larger and smaller scale granular media and the intermediate elastic solid affect nonreciprocity, given that the disparity in size of the granules of the left and right granular media affects the dominant time scales of the governing nonlinear acoustics in the granular media. Accordingly, the main cause of nonreciprocity in the interface is the excitation of low-frequency vibrations or high-frequency acoustics in the elastic solid, depending on the location and intensity of the applied shock excitation. Moreover, the passive tunability of the acoustic nonreciprocity on the intensity (energy) of the applied shock will also be explored.

This work is structured as follows. In Sec. II we introduce the model of the granular-elastic solid interface and describe briefly the computational algorithm employed in the simulations. In Sec. III we study the acoustic nonreciprocity of the interface by directly computing the granular responses when switching the excitation and measurement points. Following this study, we systematically analyze wave transmission in the elastic solid in Sec. IV and show that depending on the location of the applied shock and the governing time scales of the granular acoustics, the elastic solid undergoes either vibrations (standing waves—vibration modes) or acoustics (traveling waves). Last, in Sec. V we summarize the main results of this work and discuss their potential applications.

II. SYSTEM DESCRIPTION

We consider the hierarchical 2D granular-solid interface shown in Fig. 1. It is composed of two hexagonally packed, initially uncompressed granular media, on the left with larger-size granules and on the right with smaller-size granules, separated in the middle by a thin elastic solid; this will be modeled either as a thin elastic plate or as a slender Euler-Bernoulli beam. The two left and right granular media are hierarchical in the sense that both are composed of 14 identical granules which, however, differ in size. Three of the four boundaries of each granular medium are clamped, as

are the lateral boundaries of the intermediate elastic solid; cf. Fig. 1(b). For simplicity, we refer to the three components of the granular-solid interface as the large-scale granular medium (LSGM), the elastic solid, and the small-scale granular medium (SSGM), respectively. This interface is excited from the free edge of either the LSGM or SSGM by a shock excitation. Moreover, the granular-solid interface is assumed to be at rest before the excitation is applied. In this work, we discuss only a special symmetric case, where the excitation is applied to the middle granule of the boundary perpendicular to the elastic solid; however, the computational formulation applies to more general excitation scenarios, including asymmetric and general transient excitations.

Moreover, to simplify the mathematical model we assume that all granular motions are planar; in addition, assuming that the intermediate elastic solid is sufficiently thin we consider the plane stress approximation for the equations of infinitesimal linear elasticity governing its dynamics, so the that its corresponding deformations are also planar. Following the models in the previous works [23,24], the discrete element (DE) method is applied to model the acoustics of the left and right granular media, and the finite element (FE) method is applied to model the elastic solid. The two computational models are decoupled by accurately computing the interaction forces that couple the discrete (granular) and continuum (elastic solid) components of the interface at successive time steps [23,24]. Last, the conservation of total energy—including dissipative effects—is monitored at each time step to verify the accuracy and validity of the algorithm.

A. Discrete element (DE) modeling of the granular media

Both the LSGM and SSGM are composed of 14 identical, spherical granules that are in point contact with each other without prior compression before the excitation is applied. Each granule interacts with its neighbors and/or the elastic plate through Hertzian normal interactions with normal (viscous) dissipative and tangential frictional forces which are caused by granule rotations. Hence, even though each granule is assumed to be linearly elastic, the granular media are governed by strongly nonlinear (in fact, nonlinearizable) acoustics due to the geometric nonlinearities developing at the contact points. Under certain assumptions related to small elastic deformations [38–40], each granule is approximated as a rigid body with three planar degrees of freedom (DOF), i.e., two translational DOFs and one rotational DOF. The model of 2D granular interactions developed in [29] is adopted in this work as well; it incorporates the Hertzian model for normal interactions and a continuous Coulomb-tanh friction model for tangential (frictional) interactions.

In the DE model, the equations of motion of a single granule are given by [note that unless otherwise noted bold symbols denote (2×1) vectors]

$$m_i \ddot{\boldsymbol{s}}_i = \sum_j (\boldsymbol{N}_{ij} + \boldsymbol{f}_{ij}) + \sum_k (\boldsymbol{N}_{ik} + \boldsymbol{f}_{ik}),$$

$$I_i \ddot{\boldsymbol{\theta}}_i = \sum_j (R_i \boldsymbol{n}_{ij} \times \boldsymbol{f}_{ij}) + \sum_k (R_i \boldsymbol{n}_{ik} \times \boldsymbol{f}_{ik}), \quad (1)$$

where m_i, R_i, and I_i denote the mass, radius, and the moment of inertia of the ith granule, respectively; specifically,

$I_i = \frac{2}{5} m_i R_i^2$ for spherical granules. Also, $\boldsymbol{s}_i$ denotes the displacement vector of the center of the ith granule, and $\boldsymbol{\theta}_i = \theta_i \boldsymbol{k}$ the angular rotation pseudovector of the ith granule, where θ_i denotes the rotation amplitude and $\boldsymbol{k}$ the unit pseudovector with anticlockwise rotation designated as the positive direction. Overdot denotes differentiation with respect to the time variable τ. As shown in Fig. 1(c), $\boldsymbol{N}_{ij}$, $\boldsymbol{f}_{ij}$ are the normal and tangential forces exerted to the ith granule by the jth granule, respectively, whereas $\boldsymbol{N}_{ik}$, $\boldsymbol{f}_{ik}$ denote the normal and tangential forces applied on the ith granule by the kth contact point with the thin plate, respectively. In (1) $\boldsymbol{n}_{ij}$ denotes the unit position vector between granules that points from the center of the ith granule to the center of the jth granule and is given by $\boldsymbol{n}_{ij} = (\boldsymbol{s}_j - \boldsymbol{s}_i)/|\boldsymbol{s}_j - \boldsymbol{s}_i|$; similarly, $\boldsymbol{n}_{ik}$ denotes the unit position vector between a granule and a contact point at the edge of the thin plate, pointing from the center of the ith granule perpendicular to the kth contact point on the edge of the plate.

The normal force $\boldsymbol{N}_{ij}$ generated from the compressive interaction between the ith and jth granules obeys the Hertzian law [25,39,40] with viscous dissipation,

$$\boldsymbol{N}_{ij} = -\left(A_{ij} \delta_{n,ij}^{3/2} + \gamma_{ij} \dot{\delta}_{n,ij}\right) \boldsymbol{n}_{ij}, \quad (2)$$

where $\delta_{n,ij}$ denotes the relative normal deformation between the ith and the jth granules given by $\delta_{n,ij} = \max(R_i + R_j - |\boldsymbol{s}_j - \boldsymbol{s}_i|, 0)$. Note that $\delta_{n,ij}$ is greater than zero only if the distance $|\boldsymbol{s}_j - \boldsymbol{s}_i|$ between the centers of the granules at the current time instant is smaller than the distance between these centers at the initial state when the granules are in contact without compression. Otherwise, the granules lose contact and the normal force $\boldsymbol{N}_{ij}$ is zero. The elastic and damping coefficients A_{ij} and γ_{ij} are dependent on the material properties of the granules, the sizes of the granules, and the relative normal deformation $\delta_{n,ij}$,

$$A_{ij} = (4/3) E_{ij}^* \sqrt{R_{ij}^*}, \quad \gamma_{ij} = \alpha_n (m_{ij}^* A_{ij})^{1/2} \delta_{n,ij}^{1/4}, \quad (3)$$

where α_n is a constant coefficient related to the restitution coefficient [39], and E^*, R^*, and m^* denote the effective Young's modulus, effective radius, and effective mass, respectively. These are defined as

$$\frac{1}{E_{ij}^*} = \frac{1 - \nu_i^2}{E_i} + \frac{1 - \nu_j^2}{E_j},$$

$$\frac{1}{R_{ij}^*} = \frac{1}{R_i} + \frac{1}{R_j}, \quad (4)$$

$$\frac{1}{m_{ij}^*} = \frac{1}{m_i} + \frac{1}{m_j},$$

where $E_{i(j)}$, $\nu_{i(j)}$, $R_{i(j)}$, and $m_{i(j)}$ denote the elastic modulus, Poisson ratio, radius, and mass of the $i(j)$th granule, respectively.

The Hertzian model with viscous dissipation (2) also applies for the contact between a granule and the boundaries of the elastic solid or the lateral fixed walls by replacing the normal relative deformation $\delta_{n,ij}$ by the relative normal deformation $\delta_{n,ik}$ between the center of the granule and the corresponding boundary [cf. Fig. 1(c)]. The corresponding unit normal vector $\boldsymbol{n}_{ij}$ is also replaced by the unit normal

vector n_{ik}. We assume that the clamped boundaries of the rigid walls are rigid and therefore $E_k \to +\infty$, $R_k \to +\infty$ and $m_k \to +\infty$, which yields $E_{ik}^* = \frac{E_i}{1-v_i^2}$, $m_{ik}^* = m_i$, and $R_{ik}^* = R_i$ at the contact points between the granules and the three clamped boundaries. To determine the effective mass m_{ik}^*, modulus E_{ik}^*, and radius R_{ik}^*, for the flexible boundaries with the elastic solid we assume that a small, flat, massless, rigid layer is perfectly bonded to the edge of the elastic solid at the kth contact point; this helps to overcome any inconsistencies in the contact between a granule and an elastic body [29,41]. Since the rigid layer is flat, massless, and rigid, it holds that $E_k \to +\infty$, $R_k \to +\infty$, and $m_k \to 0$. In this case the coefficients A_{ik} and γ_{ik} are defined similarly to Eq. (3) with $E_{ik}^* = \frac{E_i}{1-v_i^2}$, $m_{ik}^* = 0$, and $R_{ik}^* = R_i$ (given that the flat boundary of the thin plane has infinite radius of curvature).

The Hertzian model is valid for frictionless granular contacts under purely compressive interactions. Considering the effect of friction, for (typically) small friction coefficients the magnitudes of the tangential forces are much smaller than the normal forces. In this case, shear deformations of the granules can be neglected, and so the Hertzian model is still applicable. A continuous (smooth) Coulomb-tanh model [42,43] is adopted to model the tangential forces applied to the granules, yielding the following frictional force applied to the granules (cf. Fig. 10 in Appendix B):

$$f_{ij} = -\mu |N_{ij}| \tanh(k_s \dot{\delta}_{t,ij}) t_{ij}, \tag{5}$$

where μ denotes the friction coefficient of the Coulomb model, k_s is a coefficient that determines the smoothness of the Coulomb-tanh model, t_{ij} denotes the unit vector in the tangential direction of the contact given by $t_{ij} = k \times n_{ij}$, and $\dot{\delta}_{t,ij}$ is the relative tangential velocity between interacting granules (between a granule and the kth contact point on the edge of the plate) given by

$$\dot{\delta}_{t,ij} = [(\dot{s}_i + R_i \dot{\theta}_i \times n_{ij}) - (\dot{s}_j + R_j \dot{\theta}_j \times n_{ji})] \cdot t_{ij}. \tag{6}$$

Clearly, the friction model (5) is also applicable for the tangential force f_{ik} between a boundary granule and the thin plate by replacing the relative tangential velocity between granules, $\dot{\delta}_{t,ij}$, with the relative tangential velocity $\dot{\delta}_{t,ik} = [(\dot{s}_i + R_i \dot{\theta}_i \times n_{ij}) - \dot{u}_{ki}] \cdot t_{ik}$ between the contact granule and the plate.

Compared to the discontinuous Coulomb friction model, the Coulomb-tanh model provides a continuous relation between the friction force and the relative tangential velocity which as discussed in [27] is beneficial for the numerical stability of the computational algorithm. When the magnitude of the relative tangential velocity $\dot{\delta}_{t,ij(ik)}$ is large, the tanh term approaches the limits of ± 1 and converges to the Coulomb model. Moreover, when the relative tangential velocity $\dot{\delta}_{t,ij(ik)}$ is small, Eq. (5) converges to the viscous damping model. It follows that the introduction of the coefficient k_s in the numerical simulation represents a trade-off between the numerical stability and the convergence of the friction force to the Coulomb model. On the one hand, large values of k_s make the Coulomb-tanh model converge to the Coulomb model, but at the same time they render the computations difficult to converge and to require very small time steps and prohibitive

computational effort. Therefore, a proper choice for k_s ensures that $k_s v_{ch} \gg 1$, where v_{ch} is the characteristic velocity for the acoustics [27]. In that case, the Coulomb-tanh frictional model captures successfully the dissipative effects of friction in the granular-elastic solid interface and approximates well the Coulomb model [29].

B. Finite element (FE) modeling of the intermediate elastic solid

In this work the intermediate elastic solid will be modeled in two different ways: either as a *thin elastic plate* or a *slender Euler-Bernoulli beam*. The rationale behind this dual model approximation is to study the efficacy of the simpler beam model or the more accurate plate model to capture the strongly nonlinear and highly discontinuous acoustics of the granular interface of Fig. 1; moreover, given the expected improved accuracy of the plate model, we wish to investigate the limit of applicability of the simpler (and less computationally expensive) beam model on capturing the transient stress wave scattering at the interfaces of the elastic solid with the left and right granular media.

We consider first the thin plate model. As in [27], in this work we consider the case where the thickness of the intermediate plate is much smaller than its length or width, so that the plane stress approximation is applicable [44]. In this case, the 3D infinitesimal linear elasticity equations for the plate model is adopted but with stress components $\sigma_z = \sigma_{xz} = \sigma_{yz} = 0$, where the z denotes the thickness direction. The plane-stress assumption yields 2D governing equations of motion, which are compatible with the 2D DE equations governing the granular media,

$$\rho(\ddot{u}_x, \ddot{u}_y)^T = \left(\frac{\partial \sigma_x}{\partial x} + \frac{\partial \sigma_{xy}}{\partial y}, \frac{\partial \sigma_{xy}}{\partial x} + \frac{\partial \sigma_y}{\partial y} \right)^T,$$

$$(\varepsilon_x, \varepsilon_y, \gamma_{xy})^T = \left(\frac{\partial u_x}{\partial x}, \frac{\partial u_y}{\partial x}, \frac{\partial u_x}{\partial y} + \frac{\partial u_y}{\partial x} \right)^T,$$

$$(\sigma_x, \sigma_y, \sigma_{xy})^T = \frac{E}{1-v^2} \begin{pmatrix} 1 & v & 0 \\ v & 1 & 0 \\ 0 & 0 & (1-v)/2 \end{pmatrix} (\varepsilon_x, \varepsilon_y, \gamma_{xy})^T, \tag{7}$$

where (u_x, u_y) denotes the displacement vector, $\varepsilon_x, \varepsilon_y, \gamma_{xy}$ the normal and shear strains, respectively, and $\sigma_x, \sigma_y, \sigma_{xy}$ the normal and shear strains, respectively. In (7) E, v, and ρ denote the Young's modulus, Poisson's ratio, and density of the material of the thin plate. Note that the effects of dissipation are not considered in (7), since the (linear) wave propagation in the solid medium is much faster than the (nonlinear) wave propagation in the granular media [29]; in addition, selecting a thin plate made of steel ensures very small levels of structural (internal) dissipation so the lossless assumption for the thin plate is justified.

The boundaries of the plate are either free or clamped except for its contact points with the boundary granules of the LSGM and the SSGM; cf. Fig. 1. Accordingly, the boundary condition at a clamped boundary is $(u_x, u_y) = (0, 0)$, while at the free boundary is $\sigma \cdot n = (0, 0)$, where σ denotes the 2D stress tensor and n the outward unit normal vector at the edge of the plate. However, at a contact point with a

granule, the contact area is assumed to be circular, and the plate deformation is not uniform along the thickness direction. Therefore, the plane stress assumption is not assumed to hold at the contact points between the granules and the plate. To overcome this inconsistency, we assume that the small rigid layers bounded to the plate cover the thickness direction so that the plate deformation along the thickness direction is assumed to be uniform; in that case only translational and rotational motions are allowed for the rigid layers. Moreover, given that the deformation of the plate at a contact point is assumed to be small, the contact forces exerted to the plate by the contacting granule are approximately applied at the middle of the rigid layer, and the directions of the normal and tangential unit vectors at the interface, $\boldsymbol{n}_{ik}$ and $\boldsymbol{t}_{ik}$, are invariant [cf. Fig. 1(c)]. Under these conditions, the normal and tangential forces between the granules and the plate at the contact points are distributed by the rigid layers so that the plane-stress condition is approximately satisfied.

We note that St. Venant's principle guarantees that the small rigid layers do not have any significant effect on the far-field acoustical response of the plate. However, if the length of the rigid layer approaches zero, the displacements of the rigid layer diverge to infinity; hence, to overcome this inconsistency, it is necessary to select appropriately the length of the rigid layer in order to avoid the singularities associated with a concentrated force. Accordingly, the length of the rigid layer is selected as $R/10$, where R denotes the radius of the granule in contact with the plate. This value is comparable to the contact diameter at the interface, which leads to reasonable results [29].

The finite element (FE) method is applied to discretize the plate and solve the 2D planar plane stress infinitesimal elasticity (7). To this end, eight-node quadrilateral isoparametric elements are employed in the FE discretization. Moreover, multipoint constraints are imposed upon the nodes on the rigid layers since only rigid body motions are allowed for these components. The translational DOFs (in the x and y directions) of the node at the middle point of each rigid layer as well as the rotational DOF of the rigid layer are considered as driven DOFs, so that all other DOFs of the nodes on the rigid layer can be expressed as linear combinations of the driven DOFs. Therefore, the (linear) equations of motion of the discretized plate (incorporating the rigid layers at the contact points with the granules as well as the clamped boundary conditions) can be expressed as follows:

$$M\ddot{x} + Kx = F \tag{8}$$

where $\boldsymbol{K}$ and $\boldsymbol{M}$ denote the stiffness and mass matrix of the FE model, respectively, $\boldsymbol{x}$ the displacement vector of the corresponding generalized displacements and rotations at the nodes of the plate, and $\boldsymbol{F}$ the force vector that incorporates the contact forces exerted at the contact points by the interacting granules of the LSGM and SSGM. Since these forces are applied only at the middle nodes of the rigid layers, $\boldsymbol{F}$ is a sparse vector, composed of the normal and shear forces applied at the middle points of the rigid layers given by (2) and (5). Clearly, the displacement vector $\boldsymbol{u}_k$ at the kth contact point is identical to the translational displacements at the middle nodes of the corresponding rigid layer at that contact point.

As mentioned previously, an alternative simpler (and less computationally demanding) model considered for the thin elastic solid is a slender Euler-Bernoulli beam, based on the fact that it has small width compared to its lateral dimension. In considering this alternative model we wish to perform a comparative study of the effects of the different modeling of the intermediate elastic solid on the overall nonlinear acoustics of the integrated granular-solid interface. To this end, and keeping the notation introduced for the plate, the following Euler-Bernoulli beam model is considered:

$$\rho A \frac{\partial^2 u_x}{\partial t^2} + EI \frac{\partial^4 u_x}{\partial y^4} = f, \tag{9}$$

where ρ and E denote the density and Young's modulus of the beam, respectively, A its cross section, I the second moment of area of the cross section about the bending axis, and f the contact force distribution provided by the interactions of the beam with the contacting granules of its left and right. In this case—contrary to the previous plate model (7)—the axial deformation, u_y, is neglected since the axial rigidity is assumed to be much larger than the flexural rigidity. Complementing (9) are the standard boundary conditions $u_x = 0$ and $\frac{\partial u_x}{\partial y} = 0$ at the clamped lateral boundaries.

As mentioned, the distributed force f is dependent on the beam-granule interactions. Different from the plate model, however, the response of the beam is finite even subject to a concentrated force. Therefore, the contact forces are assumed to be directly applied to the neutral axis of the beam as concentrated loads. Under this assumption, the tangential forces do not induce any deformations of the beam. The normal forces and the tangential forces are also computed by (2) and (5), respectively, where the displacement vector at the edge of the beam $\boldsymbol{u}_k$ is approximated by the vector of deformations of the neutral axis at the contact points.

To discretize this alternative beam model, the deflection u_x is interpolated through the use of a cubic function. The resulting discretized equation of motion has a form similar to (8), however, with different displacement vector $\boldsymbol{x}$, force vector $\boldsymbol{F}$, stiffness matrix $\boldsymbol{K}$, and mass matrix $\boldsymbol{M}$. Compared with the plate model, the force vector $\boldsymbol{F}$ is also a sparse vector containing the normal interaction forces as its only nonzero elements.

C. Coupling forces at the granular-elastic solid interfaces

In synopsis, the governing equations of motion of the granular-solid interface of Fig. 1 are Eqs. (1) and (8) which are coupled by the normal (Hertzian elastic with viscous dissipation) and tangential (frictional) interaction forces at the contact points between the LSGM and SSGM and the elastic solid. Given the large disparity of the DOFs of the linear FE (8) and the nonlinear DE (1), these are solved separately. Key to this computation is the accurate computation of the highly discontinuous, nonlinear coupling forces. This is accomplished through a robust iterative-interpolative computational algorithm whose basic elements are discussed in Appendixes A and B, and more details can be found in [27]; here we provide only a brief synopsis.

The β-Newmark method is used to solve the FE (8), while the Runge-Kutta method is employed to solve the DE (1).

The most critical step of the computation is the accurate computation of the interaction forces at the interface between the granular media and the elastic solid at each time step. To this end, a nonlinear map is generated, iterating the vector of normal and tangential interaction forces at each time step of the computation, until convergence is reached; details of this map are given in [27], and the main steps of the algorithm are summarized in Appendix A. Note that when the plate model is considered, the nonzero terms in the interaction force vector $\boldsymbol{F}$ in (8) involves the friction force as well, which is not involved in the beam model. Since the friction force is highly sensitive to the relative tangential velocity, a stability analysis is necessary for the convergence of the nonlinear map for the case of the plate model. With a few assumptions [27], the nonlinear map of the interaction force vector can be divided into several local maps, each corresponding to a separate contact point (cf. Appendix A and [29]). Assuming an adaptive (variable) time step $\Delta\tau$ for the computation, a pair of linearized eigenvalues for each of the local maps is analytically computed, and the following approximate stability criterion is formulated ensuring stability of the computation of the friction forces at the interface with the plate:

$$
\begin{aligned}
|\lambda_{ki,t}| = \tfrac{1}{2}\, \mu\, k_s |N_{ik}|\, \Delta\tau\, \boldsymbol{T}_{i,t}\big(\boldsymbol{M} + \tfrac{1}{4}\boldsymbol{K}\Delta\tau^2\big)^{-1}\boldsymbol{T}_{i,t}{}^T \\
\times \cosh^{-2}(k_s\dot{\delta}_{t,ik,s}) < 1.
\end{aligned}
\tag{10}
$$

In the above criterion $\lambda_{ki,t}$ denotes the linearized eigenvalue of the local map at the kth contact point at the interface, corresponding to the iteration of the friction force between the ith granule and the edge of the plate (it turns out that the corresponding linearized eigenvalues associated with the iterations of the normal interaction forces are always less that unity in modulus). In (10) $\boldsymbol{T}_{i,t}$ denotes a sparse vector that has only one nonzero element with unit value located at the tangential driven DOF of the rigid layer at the kth contact point. Whenever the modulus of the linearized eigenvalue, $|\lambda_{ki,t}|$, tends to reach unity, the time step is varied (adapted) to ensure that the stability criterion (10) is satisfied. Specifically, from (10), the modulus $|\lambda_{ki,t}|$ is proportional to the time step $\Delta\tau$. Therefore, the self-adaptive algorithm introduced in [29] is followed, yielding a critical time step $\Delta\tau_{cr}$ at each time step of the computation; then, by selecting the time step increment $\Delta\tau < \Delta\tau_{cr}$ convergence of the simulation is achieved; an example of the use of adaptive steps to impose the criterion (10) is given in Appendix B. By applying this computational protocol for all contact points at both edges of the plate (i.e., at the interfaces with the left LSGM and right SSGM), the convergence of the computational algorithm is achieved and numerical instabilities are robustly eliminated from the computation.

Last, energy measures are also computed to provide an overall (global) indicator for convergence of the computational algorithm at each time step. To this end, we compute the instantaneous energy of each component of the interface (i.e., the LSGM, the intermediate elastic solid, and the SSGM) in order to study the energy transmission through, and scattering at the interface, and also verify the accuracy and robustness of the simulation. The energy of each component is evaluated as

follows:

$$
E_e = \frac{1}{2}\dot{\boldsymbol{x}}_e^T \boldsymbol{M}_e \dot{\boldsymbol{x}}_e + \frac{1}{2}\boldsymbol{x}_e^T \boldsymbol{K}_e \boldsymbol{x}_e,
$$

$$
E_{gi} = \frac{1}{2}m_i|\dot{\boldsymbol{s}}_i|^2 + \frac{1}{2}I_i\dot{\theta}_i^2 + \frac{1}{5}\sum_j A_{ij}\delta_{n,ij}^{5/2} + \frac{2}{5}\sum_k A_{ik}\delta_{n,ik}^{5/2},
$$

$$
E_{p(b)} = \sum E_e = \frac{1}{2}\dot{\boldsymbol{x}}^T \boldsymbol{M}\dot{\boldsymbol{x}} + \frac{1}{2}\boldsymbol{x}^T \boldsymbol{K}\boldsymbol{x},
$$

$$
E_g = E_{g,LS} + E_{g,SS} = \sum_{i\in LS} E_{gi} + \sum_{i\in SS} E_{gi},
\tag{11}
$$

where $E_{p(b)}$ denotes the instantaneous energy of the elastic plate (beam), E_e the instantaneous energy of an element of the plate (beam), E_g the instantaneous energy of the granular system, E_{gi} the total instantaneous energy of a granule, and $E_{g,LS}$ and $E_{g,SS}$ the instantaneous energies of the LSGM and SSGM, respectively. The vector $\boldsymbol{x}_e$ and matrices $\boldsymbol{M}_e$ and $\boldsymbol{K}_e$ denote the nodal vector and mass and stiffness matrices, respectively, of an element of the elastic solid. Moreover, the dissipated energy is evaluated based on the work that is performed by the dissipative forces as follows:

$$
W_{\text{viscous},i}(\tau_0) = \sum_i \int_0^{\tau_0}\left[\sum_j (\gamma_{ij}\dot{\delta}_{n,ij}\,\boldsymbol{n}_{ij}\cdot\dot{\boldsymbol{s}}_i)\right.
$$

$$
\left. + \sum_k (\gamma_{ik}\dot{\delta}_{n,ik}\,\boldsymbol{n}_{ik}\cdot\dot{\boldsymbol{s}}_i)\right]d\tau,
$$

$$
W_{\text{friction},i}(\tau_0) = \sum_i \int_0^{\tau_0}\left\{\sum_j [\boldsymbol{f}_{ij}\cdot(\dot{\boldsymbol{s}}_i + R_i\dot{\theta}_i\boldsymbol{t}_{ij})]\right.
$$

$$
\left. + \sum_k [\boldsymbol{f}_{ik}\cdot(\dot{\boldsymbol{s}}_i + R_i\dot{\theta}_i\boldsymbol{t}_{ik} - \dot{\boldsymbol{u}}_k)]\right\}d\tau,
$$

$$
D(\tau_0) = -W_{\text{viscous},i}(\tau_0) - W_{\text{friction},i}(\tau_0),
\tag{12}
$$

where $W_{\text{viscous},i}(\tau_0)$ and $W_{\text{friction},i}(\tau_0)$ denote the dissipative work by the viscoelastic (structural) damping of the granule material, and the friction from the time instant 0 to time instant τ_0, and $D(\tau_0)$ denotes the total dissipated energy at time τ_0. Since the power performed by the dissipative forces is always nonpositive, the dissipated energy is always nonnegative and monotonically increasing. Considering the expressions (11) and (12), the total instantaneous energy of the granular-elastic solid interface that includes the dissipated energy, $E(\tau_0)$, should be equal to the initial impulsive energy $E_{\text{impulsive}}$,

$$
E_p(\tau_0) + E_g(\tau_0) + D(\tau_0) \equiv E(\tau_0) = E_{\text{impulsive}},
\tag{13}
$$

and be conserved at each time step of the computation after the excitation is applied. Hence, this conservation relation is an additional (global) check for the accuracy of the simulation.

III. NONRECIPROCAL ACOUSTICS OF THE GRANULAR-ELASTIC SOLID SYSTEM

In the following computational study of the nonreciprocal acoustics of the granular-elastic solid of Fig. 1, the granules and the elastic solid are composed of steel with modulus of elasticity $E = 200$ GPa, density $\rho = 7850$ kg/m^3 and
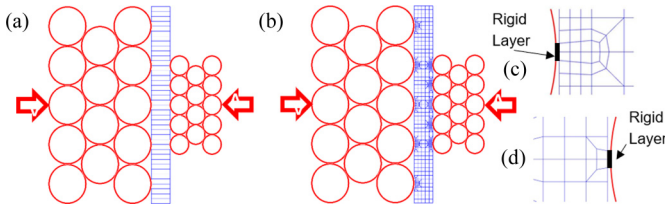
FIG. 2. Computational modeling of the granular-elastic solid interfaces: (a) FE mesh when the elastic solid is modeled as a slender Euler-Bernoulli beam—note that the contact forces are applied at nodes of the FE mesh; (b) FE mesh when the elastic solid is modeled as a thin plate—note the denser mesh close to each contact point with a granule; small rigid layer at a contact point between a granule of (c) the LSGM and (d) the SSGM and the thin plate model.

Poisson's ratio $\nu = 0.3$. Based on previous studies of the granular-solid interfaces [25,29,39,42], the friction and viscoelastic damping coefficients of the granular medium are selected as $\mu = 0.099$, $\alpha_n = 6.313 \times 10^{-3}$, and $k_s = 100$ s/m, where the notation of the previous section holds. The planar dimensions of the elastic solid medium are 0.1 m × 0.01 m, with a (small) thickness of 0.001 m. The radii of the granules of the LSGM are 0.01 m, whereas the ones of the SSGM 0.005 m. The FE mesh of the elastic solid medium is shown in Fig. 2.

For the case when the elastic solid medium is modeled as Euler-Bernouli beam, it is discretized into 40 beam elements [cf. Fig. 2(a)], whereas when it is modeled as a thin plate is discretized into 570 plate elements [cf. Fig. 2(b)]. The beam model is valid mainly for low-frequency/wavenumber vibrations (standing waves), whereas the plate model is valid for vibrations as well as higher-frequency/wavenumber acoustics (traveling waves). As such, the plate model provides a more accurate result at the expense of more computational effort due to the better modeling of the acoustics of the interface, the larger amount of DOFs and implementation of the strict convergence criterion (10).

The length of the rigid layer at each interface of a boundary granule of the LSGM and the SSGM and the elastic solid is selected as $R/10$, where R denotes the radius of the granule at the contact point. Accordingly, the FE mesh of the plate model is refined near each contact point, with two finite elements

being connected on the rigid layer as shown in Figs. 2(c) and 2(d). Since the top and the bottom boundaries of the elastic plate are clamped, the nodes on the top and bottom boundaries are fixed as well. This results in 3618 degrees of freedom in total for the plate model. The FE modeling of the slender beam model is much simpler (as no variable finite elements are needed in that case), resulting in just 78 degrees of freedom, after the boundary conditions and the multi-point constraints with the rigid layers are taken into account. This provides an indication of the simplicity and the much less computational effort required for the slender beam model.

In Fig. 3 we depict the velocity of granule 3 of the LSGM, v_{3C}, when a shock excitation is applied to granule C of the SSGM; and also the response of granule C, v_{C3}, when an identical shock excitation is applied to granule 3 (i.e., when the forcing and measurement positions are interchanged); the labeling of the granules is indicated in Fig. 1(b) and is repeated in the inset of Fig. 3(a). The intermediate elastic solid is considered to be a thin plate for this simulation, which is performed in order to highlight the nonreciprocal nature of the nonlinear acoustics of the hierarchical granular interface (since for a linear interface the responses in the two cases should be identical, i.e., $v_{3C} = v_{C3}$). The excitation consists of a half-sine pulse applied for a duration of 0.01 ms with maximum amplitude $F_{max} = 1591.6$ N [cf. Fig. 3(a); this corresponds to a high excitation intensity as discussed below]. From the responses depicted in Fig. 3(b) it is clearly seen that the interface is highly nonreciprocal. The source of this acoustic nonreciprocity can be traced in the combined effects of nonlinearity and asymmetry [34]. Indeed, nonlinearity of the interface is induced from three sources: (1) Hertzian granule-to-granule and granule-to-solid interactions, (2) collisions following separations between granules and at the granule-solid contact points, and (3) frictional effects due to granule rotations. Moreover, the symmetry of the interface is broken by the hierarchical structure of the LSGM and the SSGM. We note that the convergence of the computational results is ensured by checking and stability criterion (10) at each time step and adapting the variable time step (cf. Fig. 10 in Appendix B).

Considering the time series of the velocities v_{C3} and v_{3C} we notice an initial time lag when we compare the arrival of
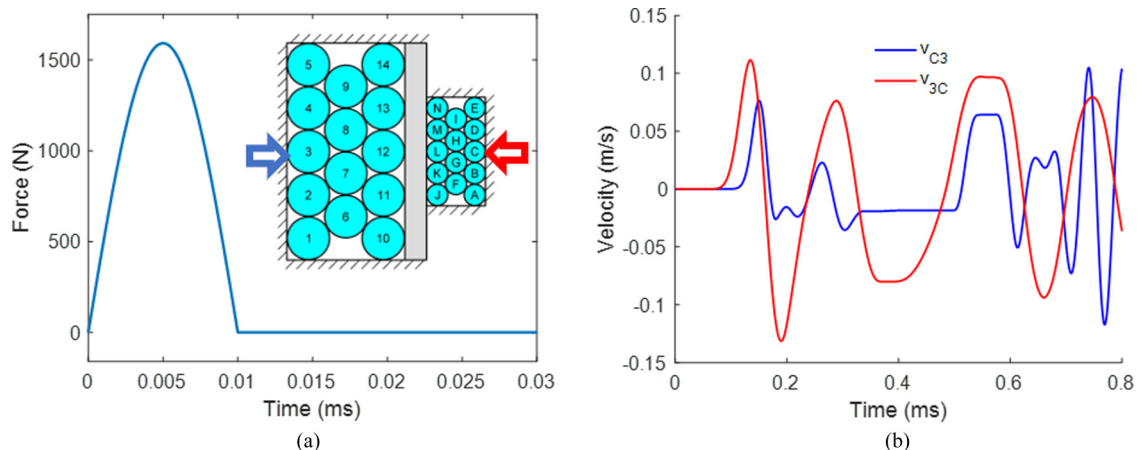

FIG. 3. Acoustic nonreciprocity in the granular-elastic solid (modeled as a plate) interface of Fig. 1: (a) The Strong shock excitation and (b) velocities of granule 3 of the SSGM, v_{3C}, and granule C of the LSGM, v_{C3}, for excitations as described in the text and in the inset of (a).

the acoustic waves in the two cases. Specifically, the earlier arrival of the pulse in granule 3 of the LSGM indicates that the acoustic waves propagate faster from right-to-left compared to left-to-right. Moreover, the frequency content appears to be different in the two time series, with a lower frequency content being noted for v_{3C} compared to v_{C3} (especially for $\tau > 0.6$ ms). We provide below a brief scaling argument that justifies the apparent difference in the wave speeds for right-to-left and left-to-right wave transmission, which should originate from the difference in scales between the LSGM and the SSGM. Indeed, since the radii of the spherical granules in the (left) LSGM are twice as large compared to the ones in the (right) SSGM, the corresponding granular masses are eight times as heavy in the LSGM compared to the SSGM. Also, since the duration of the shock excitation is extremely small, the energy of the applied shock can be estimated approximately as $E \approx I^2/m$, where I is the intensity of the applied impulse and m the mass of the excited granule; therefore, for the same shock excitation, the shock energy that is induced to the SSGM is nearly eight times as large as the corresponding shock energy induced to the LSGM. Considering that the nonlinear exponent of the Hertzian elastic interaction force between two contacting granules is $3/2 > 1$, the effective stiffness of the granular interaction increases for larger energy, i.e., it exhibits a stiffness-hardening constitutive relation, which, in turn, increases the wave speed for increasing energy [4,5,38]. This argument shows that when the shock excitation is applied to the SSGM (on the right), the resulting nonlinear acoustic wave propagates faster compared to when the excitation is applied to the LSGM (on the left); this explains the earlier arrival of the pulse in granule C of the LSGM.

As a preliminary general comment, we note that the combined effects of nonlinearity and scale asymmetry (hierarchy) in the granular interface considered yields different wave speeds for right-to-left and left-to-right wave transmission, which accounts for the time lag in the velocity signals of Fig. 3(b) and acoustic nonreciprocity. Compared to previous works which do not incorporate an intermediate elastic medium [45,46], in this work there is a novel type of nonreciprocity based on the disparity of time scales in the nonlinear acoustics of the granular media and the response of the intermediate elastic layer. Specifically, depending on the location and intensity of the applied shock, the elastic layer respond either in terms of (slow) vibrations or (fast) acoustics; accordingly, the intermediate elastic medium plays a central role in the acoustics of the entire interface as it acts as a "filter" for the frequency and wavenumber content of the waves that it transmits. To get a physical insight into the different frequency contents of the two velocity signals in Fig. 3(b) (which also contribute to the break of acoustic reciprocity) it is necessary to consider the wave scattering (transmission and reflection) at the two granular interfaces of the intermediate elastic solid with the left LSGM and the right SSGM.

Hence, we proceed to study the nonreciprocal acoustics of the granular interface when an identical shock excitation is applied either in granule 3 of the LSGM or granule C of the SSGM, generating acoustic waves propagating from left-to-right or right-to-left, respectively. To this end we consider three different shock intensities: weak, moderate, and strong.

In each case the shock excitation has the half-sine shape shown in Fig. 3(a) and is applied for a finite duration of $\tau_{exc} = 0.01$ ms; its peak forcing amplitude, F_{max}, is then selected as 63.67 N for weak, 318.3 N for moderate, and 1591.6 N for strong shock excitation [this later value corresponds to the result of Fig. 3(b)], respectively. Moreover, in our study we consider both the plate and beam models to simulate the acoustics of the intermediate elastic solid.

In Fig. 4 we depict the instantaneous normalized energies (with respect to the initial shock energy in each case) of the LSGM, the SSGM, and the elastic solid for the three shock excitations considered. In addition, we present the total normalized energy of the entire granular interface when dissipative effects (that is, viscoelastic, and frictional effects) are taken into account or when they are added to the total energy; this latter case is considered in order to verify that at each time instant the total instantaneous normalized energy sums up to 100% and, hence, ensure the accuracy of the computation. We note that in Figs. 4(a), 4(c), and 4(e) we present the results for shock excitation applied to granule 3 of the LSGM, whereas in Figs. 4(b), 4(d), and 4(f) for application of the same shock excitation (in each case) to granule C of the SSGM; in all cases considered the intermediate elastic solid is modeled either as a thin plate (solid lines), or as a simplified slender Euler-Bernoulli beam (dashed lines). Last, the total simulation time is selected as 0.8 ms in all cases, and the numerical stability of the numerical simulation is ensured by selecting adaptively the variable time step so that the convergence criterion (10) is satisfied at each time step. We note that at all shock intensity levels only a moderate portion of shock energy ends up being transmitted across the interface, for both right-to-left and left-to-right acoustic wave transmission, which highlights the efficacy of the granular interface as robust shock mitigator. In all cases, the elastic solid acts as an intermediary medium, which receives incident energy from the excited granular medium and scatters it, i.e., releases (transmits) part of this energy to the granular medium on the other side, confines (localizes) another part of this energy, and reflects the remaining part of the incident energy back to the granular medium where it is originally generated.

For the case where the shock excitation is applied to granule 3 of the LSGM [cf. Figs. 4(a), 4(c), and 4(e)], we observe clear energy transmission and reflection, and the energy transmitted in the SSGM and the energy retained (localized) in the elastic solid reach their peaks almost simultaneously. However, when the excitation is applied to granule C of the SSGM, the shock energy appears to be scattered into the whole interface. The time scale of the acoustics in this case seems to be faster compared to the previous case, and the elastic solid is excited by the propagating wavefront from the right much earlier. In addition, irrespective of the side of application of the shock the speed of the propagating wavefront (i.e., the dominant governing time scale of the nonlinear acoustics) strongly depends on the excitation level (or energy); this is anticipated for such a strongly nonlinear acoustical system. Indeed, from Fig. 4(a) (case of weak shock) we note that the wavefront initiated at the LSGM reaches the interface with the elastic solid after approximately ~ 0.2 ms, compared to ~ 0.1 ms in Fig. 4(e) corresponding to strong shock excitation from the same side.
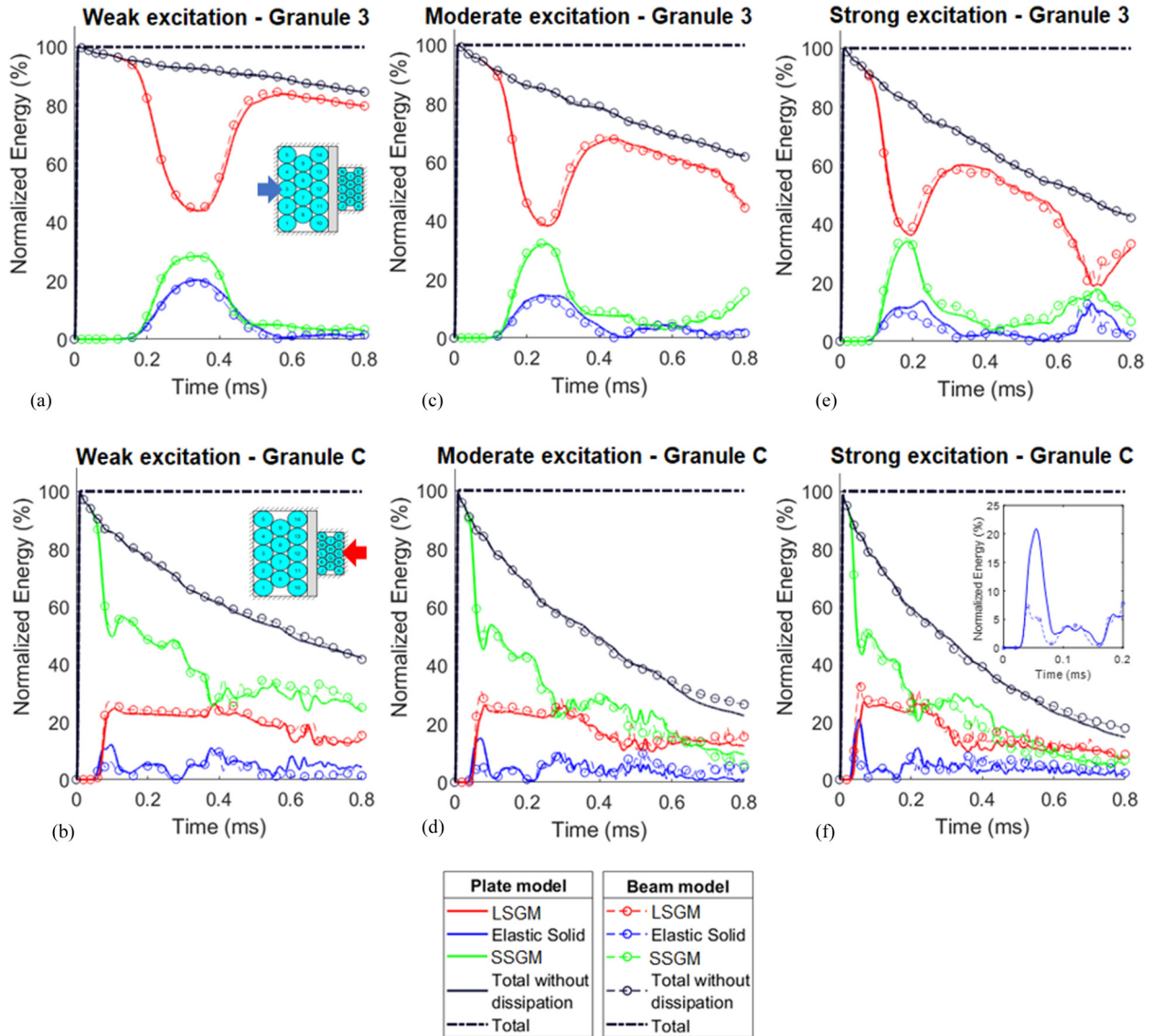
FIG. 4. Instantaneous normalized energies (with respect to impulsive energy) of the LSGM, the SSGM, the elastic solid (modeled as plate or beam), and the entire granular interface (with and without dissipation effects added): (a), (c), (e) excitation is applied to granule 3 of the LSGM for weak, moderate, and strong shocks, respectively; and (b), (d), (f) excitation is applied to granule C of the SSGM granule for weak, moderate, and strong shock excitations, respectively; the inset in (f) is an enlargement of the energy of the elastic solid in this case when modeled as plate or beam.

The same can be observed when the excitation is applied to the SSGM, e.g., compare the plots in Figs. 4(b) and 4(f). This result can be understood when one takes into account that the hardening-stiffness nonlinearity of the Hertzian granular interactions yields higher speeds for the nonlinear acoustic waves in the granular media when the energy increases. In addition, regardless of the location of the shock excitation, the higher the excitation level is, the greater is the rate of shock energy dissipation; however, the energy dissipation is larger and faster when the excitation is applied to the SSGM.

In Appendix C we provide animations of the nonlinear acoustical responses of the granular interface for weak, moderate and strong shock excitations, and for the cases when the elastic solid is modeled as a thin plate or as a slender beam. To gain better physical insight into the nonlinear acoustics of the granular interface we need to consider in more detail the

dynamics of the intermediate elastic solid when it is modeled either as a thin plate or (a simpler) slender beam. In particular, it is of interest to study how the elastic solid transmits, reflects or localizes shock energy that impedes from its left or right sides, since this will lead to a better understanding of the generation of acoustic nonreciprocity in this discrete-continuum system.

IV. SCALE DISPARITY IN THE RESPONSE IN THE INTERMEDIATE ELASTIC SOLID

The nonreciprocal acoustics of the granular interface of Fig. 1 are influenced by two main sources: First, the dissimilar wave speeds and frequency contents of the nonlinear transmitted waves (or the propagating wavefronts) in the right and left different-scale granular media; and second by the nonlinear

scattering of the propagating wavefronts at the interfaces of
the granular media with the elastic solid. The first source
of nonreciprocity is attributed to the stiffness-hardening non-
linear behavior of the granular interactions, as well as on
the scale disparity of the granule geometries of the LSGM
and SSGM, which drastically affect the initial formation and
propagation of the *primary wavefronts*, i.e., the waves that are
generated in the granular media immediately following the
applications of the shocks on the right or left. The second
source has to do with the transmission and reflection of the
primary wavefronts at the discrete-continuum interfaces when
they reach the boundaries with the elastic solid. In this section
we wish to study in detail this nonlinear scattering of the pri-
mary wavefronts and establish how it influences the acoustic
nonreciprocity.

We start by noting that based on the results of Fig. 4
the efficacy of the simplified beam model for the acous-
tics of the intermediate elastic medium can be assessed. In
Figs. 4(a), 4(c), and 4(e), it is observed that the results pre-
dicted by the beam model are in good agreement with the ones
predicted by the more accurate (and computationally expen-
sive) plate model when the shock is applied on granule 3 of the
LSGM, especially for weak and moderate shocks. By contrast
the difference between the predictions of the beam and plate
models is considerable when the shock is applied to granule C
of the SSGM; cf. Figs. 4(b), 4(d), and 4(f). Hence, for energy
transmission from the SSGM to the LSGM, the beam model
fails to accurately capture the nonlinear wave scattering at
the discrete-continuum interface, with the maximum disparity
with the plate model occurring for strong shock [i.e., when the
primary wavefront propagating from right-to-left reaches the
boundary with the elastic solid at ~ 0.05 ms; refer to the inset
in Fig. 4(f)].

The failure of the beam model to model the wave trans-
mission from the SSGM to the LSGM hints on the time
scale disparity of its response when the shock is applied to
the left or right boundaries of the interface. To gain better
physical insight into the nonlinear acoustics of the granular
interface we need to consider in more detail the response of
the intermediate elastic solid when it is modeled either as a
thin plate or (a simpler) slender beam. In particular, it is of
interest to study how the elastic solid transmits, reflects or
localizes shock energy that impedes from its left or right sides,
since this will lead to a better understanding of the generation
of acoustic nonreciprocity in this discrete-continuum system.
To highlight the difference in the dynamics of the elastic solid
when modeled as a thin plate (in plane stress) or as a slender
beam we compare snapshots of instantaneous normalized en-
ergy densities of the elastic solid for strong shock excitation
applied to either side of the granular interface. In Appendix C
we provide links to animations of the nonlinear acoustical
responses of the granular interface for weak, moderate, and
strong shock excitations, and for the cases when the elastic
solid is modeled as a thin plate or as a slender beam. To this
end, the energy density is normalized by the initial maximum
energy density of the excited granule (i.e., granule 3 of the
LSGM or granule C of the SSGM):

$$\hat{w} = \frac{w}{w_0} = \frac{E^e/V^e}{(1/2)mv_0^2}. \tag{14}$$

In (14) $\hat{w}$ and w denote the normalized and nonnormal-
ized energy density, w_0 the maximum energy density of the
excited granule, and E^e and V^e the instantaneous energy and
volume of each element (either FE for the elastic solid or
granule for the LSGM and SSGM), m the mass of the excited
granule, and v_0 the maximum instantaneous velocity of the
excited granule. Special consideration needs to be given to
the energy density of the beam element along the direction
of its width and height; this is due to the fact that, since the
finite elements of the beam are 1D, we need to perform a
2D spatial interpolation of the energy density of the beam
in order to compare it to the energy density of the plate. We
note at this point that in the Euler-Bernoulli beam model a
planar cross-section is implicitly assumed (i.e., cross sections
remain planar after deformation) and also that the normal
stress is a linear function of the beam's width. It follows
that the potential energy density is a parabolic function along
the beam's width—with the potential energy on the neutral
axis of the beam being zero. Moreover, the velocity along
the direction of the beam's height is constant, and therefore
the kinetic energy is uniformly distributed along the beam's
height. Therefore, we can compute the energy density along
the width direction of each beam element based on the FE
result, and then interpolate the energy to the height direction
based on the implicit assumption of the planar cross section.

In Fig. 5 we depict the comparison of two snapshots of
the normalized energy densities for the case of strong shock
applied to either side of the granular interface, with the elastic
solid being modeled as a thin plate or beam. The snapshots
are taken when the energy density in the elastic solid reaches
its maximum, that is, at $\tau = 0.2$ ms for left-side excitation
and $\tau = 0.05$ ms for right-side excitation. Comparing the
results of Figs. 5(a) and 5(c), we note that the wave patterns
for excitations applied to the LSGM and the SSGM are dif-
ferent. When the shock is applied to the SSGM the energy
density in the plate model indicates wave transmission from
the three middle granules of the SSGM in contact with the
elastic solid, to the corresponding three middle contacting
granules of LSGM. This reveals the excitation of a traveling
wave propagating from the right to left and the realization of
high-frequency or wavenumber acoustics in the thin plate; this
is more evident in the animations of energy densities whose
links are provided in Appendix C. However, such a traveling
wave pattern is not observed in the case of excitation from
LSGM, where the response of the thin plate is in the form of
lower frequency or wavenumber vibrations, i.e., dynamics.

This is confirmed when comparing the results of Figs. 5(a)
and 5(b): when the shock is applied to the LSGM we note that
the energy density distribution in the elastic solid predicted
by the beam model is similar to that of the plate model,
confirming the realization of vibrations. However, when the
same shock is applied to the SSGM [cf. Figs. 5(c) and 5(d)]
the beam model fails to predict the distributions of energy
densities in the elastic solid. In both cases, in the beam model
the strain is linearly distributed along the width and so the
energy density distribution is symmetric with respect to the
neutral axis of the beam (indicating vibrations); however, for
the case of the plate model the energy density is not sym-
metric with respect to the neutral axis (indicating acoustics).
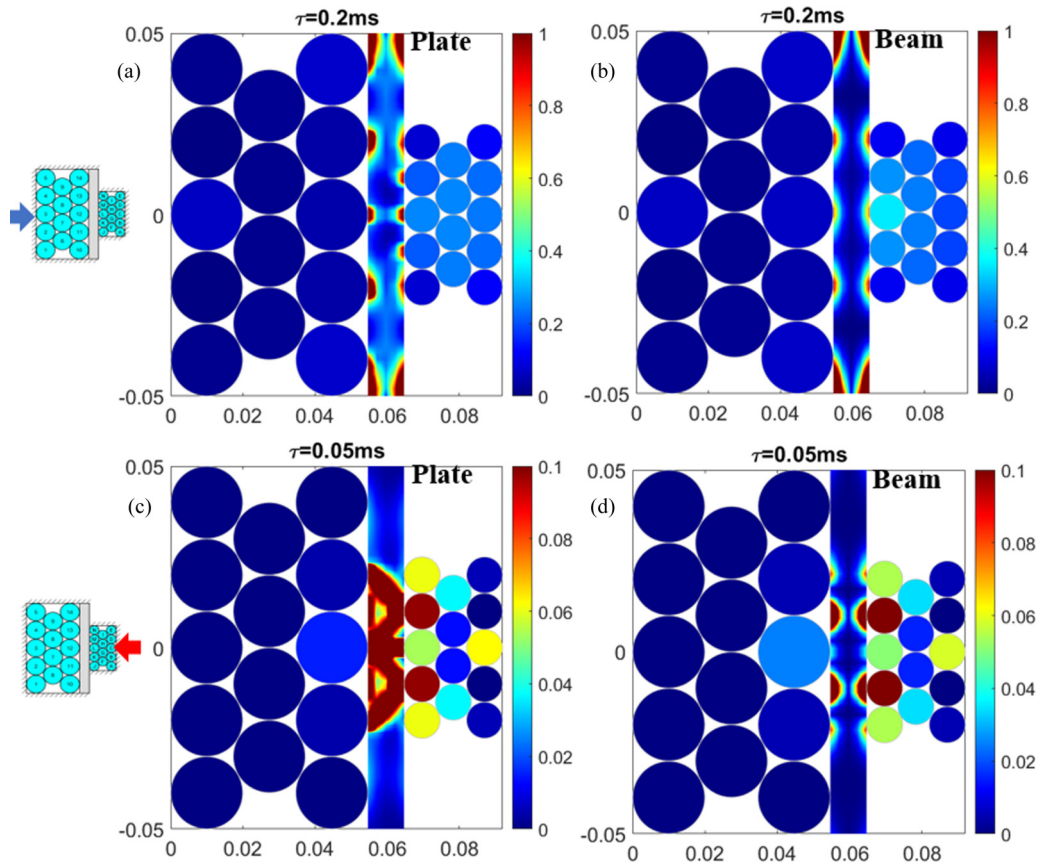In the latter case, due to the disparity in the time scales of

FIG. 5. Normalized energy density snapshots of the granular-elastic solid interface for the case of strong shock excitation: (a), (b) $\tau = 0.2$ ms with the excitation applied to granule 3 of the LSGM, and the elastic solid modeled as thin plate or Euler-Bernoulli beam, respectively; (c), (d) $\tau = 0.05$ ms with the excitation applied to granule C of the SSGM, and the elastic solid modeled as thin plate or Euler- Bernoulli beam, respectively; note the much faster acoustics in the latter case.

the responses of the contacting granules in the LSGM and SSGM, the resulting paths of the traveling waves through the elastic solid are not symmetric with respect to its neutral axis. These observations motivate us for a closer examination of the response of the elastic solid when modeled either a thin plate or a slender beam subject to the two shock scenarios shown in Fig. 5.

To this end, we hypothesize that when the shock is applied on the left (to the LSGM), the duration of the interaction forces at the interface between the LSGM and the left lateral boundary of the elastic solid is relatively long, the elastic solid performs relatively low-frequency *vibrations* where the leading bending modes with low frequency (and large wavelengths) are excited and *standing waves* are generated. On the contrary, for the same shock excitation applied to the right side (the SSGM), the acoustics is much faster, so a larger number of higher-frequency modes of the elastic solid are excited (some of which nonbending), which instead of vibrations supports *elastic wave propagation* within it at a much faster time scale (and much lower wavelengths). Hence, for shock excitation on the left the elastic solid undergoes mainly vibrations (standing waves) while for shock excitation on the right, it supports acoustics (traveling waves).

To verify this hypothesis, we analyze the frequencies, shapes and energies of the modes of the elastic solid. We

notice that all modes of the beam model are bending ones as it is governed by the Euler-Bernoulli partial differential equation. The modal analysis of the plate model shows that the first leading (lowest frequency) mode is a *bending mode* [cf. Fig. 6(b)], while the second, third, fifth, and sixth modes (sorted by their natural frequencies in the ascending order) are also bending modes and can find their analogs in the beam model of the elastic solid. However, apart from these bending modes, *the plate model also possesses families of modes that are not captured by the simplified beam model*; these are *axial* modes and *bulk* modes. In Fig. 6(c) the fourth axial mode of the plate is depicted, where the elastic solid vibrates along the vertical (axial) direction; this is the lowest frequency mode of the family of axial modes of the thin plate, which are absent from the beam mode. Also, in Fig. 6(d) the seventh bulk mode of the plate is shown, where the elastic solid is squeezed (or expanded) along the horizontal direction; again, this is the lowest frequency mode of the bulk family which is not supported by the beam model.

At this point we note that since in this work we consider only a symmetric shock excitation scenario, the fourth axial mode of the plate cannot be excited due to its antisymmetry and does not participate in the nonlinear acoustics. However, the bulk modes have a significant effect on the energy transfer. We note that the bending modes and bulk modes exhibit
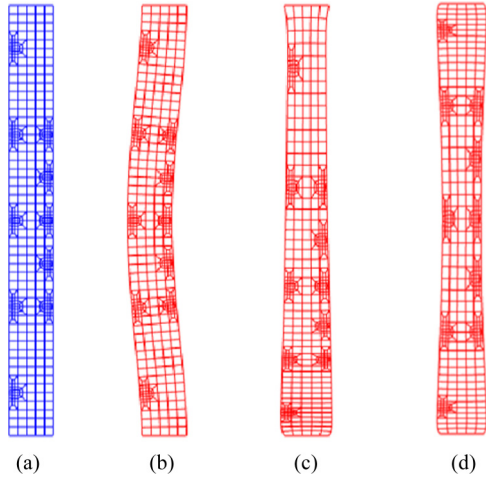
FIG. 6. Selected modes of the thin plate model of the elastic solid of the granular interface of Fig. 1: (a) Undeformed FE mesh, (b) first bending mode with natural period 0.199 ms, (c) fourth axial mode with natural period 0.0395 ms—due to its antisymmetry it cannot contribute to the acoustics, and (d) seventh bulk mode with natural period 0.0198 ms—due to its symmetry it may participate in the acoustics.

different symmetries. The bending modes exhibit antisymmetric mode shapes with respect to the neutral axis, whereas the bulk modes exhibit symmetric mode shapes. Since the energy distribution in the elastic solid at $\tau = 0.05$ ms for strong excitation from SSGM [cf. Fig. 5(c)] is asymmetric, both the symmetric axial modes and the antisymmetric bending modes are excited. It follows that if such bulk modes are excited in the plate model by the impeding wavefronts, the simplified beam model could not accurately predict the dynamics of the elastic solid, nor the nonlinear scattering of the impeding wavefronts at the boundaries with the left and right granular media. Therefore, the failure of the beam model is related to the generation of traveling waves (acoustics) in the elastic solid.

Furthermore, we investigate the family of modes excited in the acoustical response of the elastic solid by considering its instantaneous modal energies defined as follows:

$$E_{es,n} = \tfrac{1}{2}\dot{X}_n^2 \phi_n^T K \phi_n + \tfrac{1}{2}X_n^2 \phi_n^T K \phi_n, \qquad (15)$$

where $\boldsymbol{K}$ and $\boldsymbol{M}$ denote the stiffness and mass matrices, respectively, $E_{es,n}$ the energy of the nth mode of the elastic solid, X_n and $\dot{X}_n$ the corresponding modal amplitude and its derivative with respect to time, respectively, and ϕ_n the nth eigenvector.

In Fig. 7 we depict the normalized accumulated energy captured by the leading modes of the plate model and compare it to total instantaneous energy. The individual modal energies are computed by (15) and the energy normalization is performed with respect to the total energy that is induced to the system by the shock. To this end, an identical strong excitation is applied to either side of the granular interface in order to compare the convergence of the modal energy accumulation in the two excitation scenarios. In both excitation scenarios a peak of the total plate energy is observed corresponding to the arrival of the primary wavefront generated following the application of the strong shock to the LSGM or SSGM. In both cases, the amplitude of the peak is around 20% of the input energy, however, since the time scale of the acoustics for right-side excitation is faster, an earlier arrival of the primary waveform and a shorter duration of the peak is observed in that case [cf. Fig. 7(b)]. When the strong shock is applied to the left side the duration of the peak is longer and the accumulation of modal energy compared to total energy appears to be faster. Note that in Fig. 6 we showed that the leading six modes of the thin plate model consist of the leading five bending modes and an antisymmetric axial mode that has no counterpart in the thin plate model; however, that low-frequency axial mode seems not to be excited by the primary waveform (due to its antisymmetry) and so most energy is localized in the leading order bending modes. Since these modes are also predicted by the beam model, the difference of the energy distribution between the plate and the beam model shown in Figs. 5(a) and 5(b) is small. In this case, standing waves are realized, and the elastic solid mainly undergoes vibrations.

The convergence of modal accumulated energy is slower when the strong shock is applied on the right-hand side
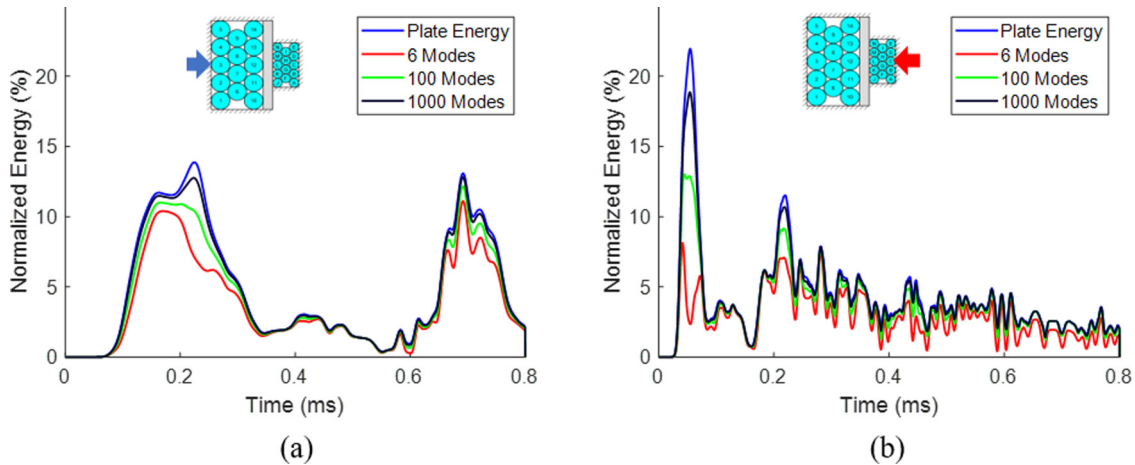

FIG. 7. Normalized accumulated modal energy in the elastic solid when modeled as a thin plate in plane stress, subject to strong shock applied (a) at granule 3 of the LSGM, and (b) granule C of SSGM; in each case the accumulated total energy and modal energies of the leading 6, 100, and 1000 plate modes are depicted as functions of time.
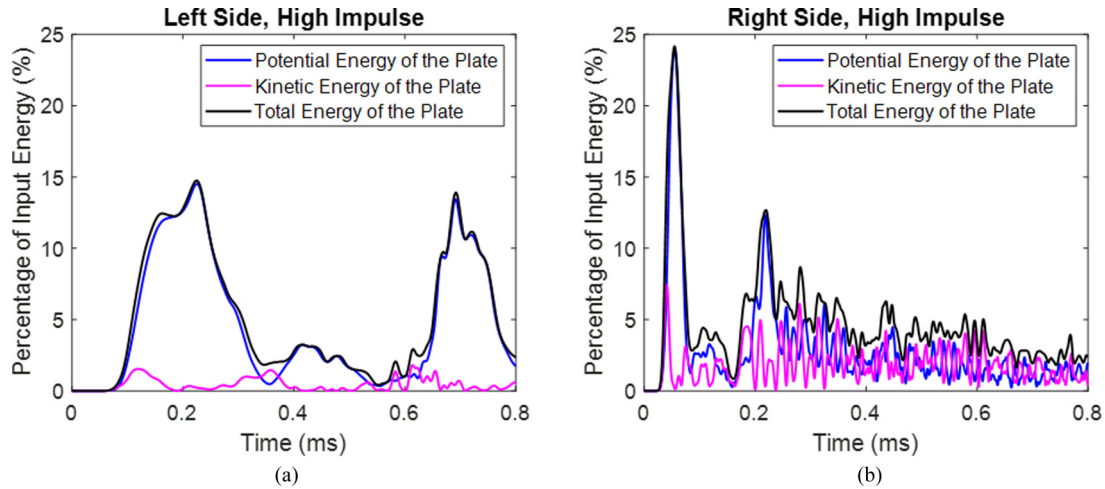
FIG. 8. Instantaneous normalized total, elastic, and kinetic energies of the elastic solid when modeled as a thin plate in plane stress subject to strong shock excitation applied to (a) granule 3 of the LSGM and (b) granule C of the SSGM.

[cf. Fig. 7(b)], indicating that the nonlinear acoustics of wave scattering at the interface of the elastic solid and the granular media is different. Indeed, in this case the plate energy reaches its early maximum at $\tau \approx 0.05$ ms, and the accumulated modal energy converges slowly to the total energy within this primary peak. With more modes being excited by the primary wavefront in this case, the convergence of modal energy in the peak is slow, even when considering as many as 1000 leading modes (a number of modes which is comparable to the total 3618 degrees of freedom of the plate model). The slow modal accumulation mainly occurs in the primary peak, since following that the convergence is seen to satisfactory. In this case the elastic solid does not merely undergo vibrations as numerous modes with large wavenumbers (or short wavelengths) are excited. Instead, we observe the occurrence of acoustics, i.e., elastic waves propagating along the width of the elastic solid when the excitation is applied to the SSGM (for links to animations showing clearly this acoustical response we refer to Appendix C). Therefore, we observe strong acoustic nonreciprocity in the granular interface for shock excitations applied to both sides: For excitation applied to the left LSGM the elastic solid (when modeled as a thin plate in plate stress) undergoes mainly (low-frequency or wavenumber) vibrations, whereas for an identical excitation applied to the right SSGM it undergoes (high-frequency or wavenumber) acoustics. To the authors' best knowledge this is the first report of a nonreciprocal system which, depending on the location of the applied shock excitation, undergoes either vibrations (standing waves) or acoustics (traveling waves). The source of nonreciprocity is the strong nonlinearity of the granular media in synergy to the asymmetry caused by the different scale composition of the left and right granular media.

Considering that the length of the plate model of the elastic solid is 0.1 m and its width 0.01 m, the resulting slenderness ratio is small so the natural frequencies of the leading axial and bulk modes are comparable to the natural frequencies of the lowest bending modes. Specifically, the natural period of the first (bending) mode of the plate model is 0.199 ms, while that of the seventh (bulk) mode is 0.0198 ms (the antisym-

metric lowest axial mode does not participate in the acoustics due to the symmetry of the applied shock excitation). Clearly, the accuracy of the beam model is dependent on whether the leading bending modes are dominant in its response, which, in turn, is determined by the dominant time scales of the impeding wavefronts, and of the granular-elastic solid interaction. As mentioned previously [4,5], subject to the same shock applied to either side of the granular interface, the resulting propagating primary wavefront in the SSGM is much faster compared to the one transmitted in the LSGM. This means that that the time scales governing the nonlinear scattering of the wavefront at the granular-solid interface are much faster when the shock is applied to the right (SSGM is excited). In turn, this results in the excitation of a higher range of modes of the elastic solid, over a wider range of frequencies. Therefore, the bulk modes and the traveling waves are excited, and the simplified beam model does not agree with the plate model. For the shock applied to the LSGM, the time scales governing the nonlinear scattering of the wavefront at the granular-solid interface are relatively slow, and therefore only the leading bending modes of the elastic solid are excited (in the form of standing waves), so the simplified model agrees well with the plate model.

The slenderness ratio of the intermediate elastic solid is also critical factor. For larger slenderness ratios, the natural frequencies of the leading bulk modes are much larger than the natural frequencies of the leading bending modes. In this case, the elastic solid acts as a beam and only standing waves are excited (involving the bending modes) irrespective of the location of the applied shock (left or right). However, for smaller slenderness ratios, traveling waves are initiated and the beam model fails irrespective of the location of the shock. Therefore, the previously discussed time scale disparity of the nonlinear acoustics depends also on the slenderness ratio of the intermediate elastic solid.

Another interesting aspect of the nonreciprocal acoustics is gained by studying the partition of the instantaneous total energy of the elastic solid in terms of kinetic and potential energies. In Fig. 8 we depict the normalized kinetic, potential, and total energies of the elastic solid when modeled
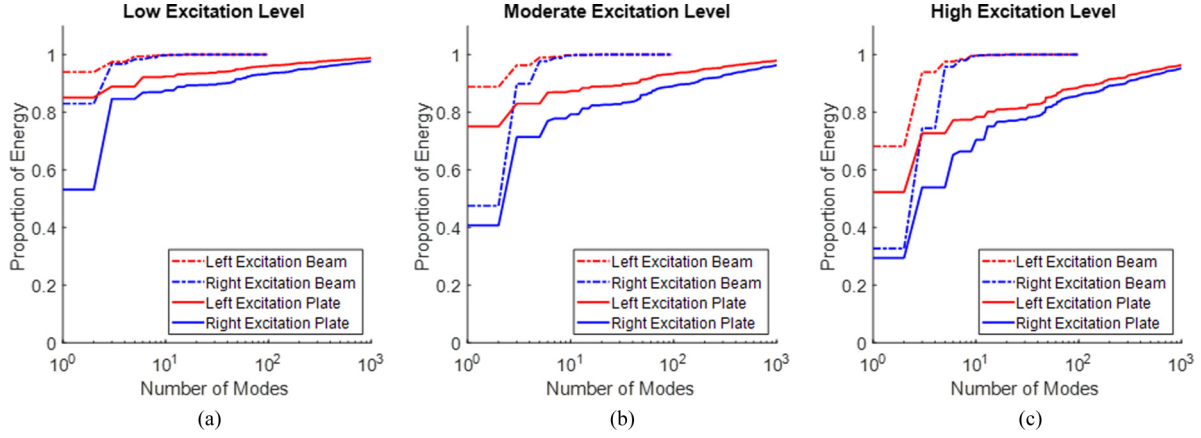
FIG. 9. Accumulated energy captured by the leading modes, as defined in (16): (a) weak ($F_{\max} = 63.67$ N), (b) moderate ($F_{\max} = 318.3$ N), and (c) strong ($F_{\max} = 1591.6$ N) shocks.

as a thin plate in plane stress, with the same strong shock excitations applied on either side. With the excitation applied to the LSGM [cf. Fig. 8(a)] the potential energy overweighs the kinetic energy throughout the duration of the response of the elastic solid. Given that the natural period of the first bending mode of the plate is ~ 0.2 ms, i.e., comparable with the duration of the primary (main) peak, the elastic solid is excited "pseudostatically" predominantly in its first bending mode, and, as mentioned previously undergoes relatively low-frequency vibrations. This provides another evidence that the standing waves are generated with the excitation from LSGM. However, a different picture is obtained when the excitation is applied to the SSGM [cf. Fig. 8(b)], where the potential energy overweighs the kinetic energy only in the primary peak, which in this case is much shorter in duration compared to the previous case; this indicates that more modes than the fundamental bending ones are now excited by the imping-ing primary wavefront; this confirms the acoustical (rather than vibrational) response of the elastic solid in this case. Moreover, note that after the main peak, the elastic solid con-tinuously exchanges kinetic and potential energies resembling a "global oscillator" effect [29]. This behavior opens the way for conceiving nonreciprocal systems with response features dominated by either vibrations or acoustics, depending on the location of the excitation shock. In turn, this can enhance the capacity of such systems to passively confine and locally dissipate a significant portion of input shock energy at a given frequency range, examples of which have been demonstrated theoretically and experimentally in previous studies [47,48].

Last, we study the dependence of the acoustic nonreciproc-ity of the granular interface on the level of the shock. To this end, we consider the half-sine pulse excitation depicted in Fig. 3(a) with the aforementioned three levels of forcing amplitude, $F_{\max} = 63.67$ N, 318.3 N, and 1591.6 N, cor-responding to weak, moderate, and strong excitation levels, respectively, and fixed shock $\tau_{\text{exc}} = 0.01$ ms. In Fig. 9 we depict 12 cases of shock excitation applied either from the left (at granule 3 of the LSGM) or the right side (granule C of the SSGM) of the granular interface, and with the intermediate elastic solid being modeled either as a thin plate or a slender beam. In these plots we consider the normalized accumulated energy captured by the leading $1 < N < 10^3$ modes of the

elastic solid for each excitation scenario, averaged over time as follows:

$$\sum_{n=1}^{N} \frac{\int_0^{\tau_0} E_{es,n} d\tau}{\int_0^{\tau_0} E_{es} d\tau}. \qquad (16)$$

In (16) $E_{es,n}$ denotes the modal energy of the $n-th$ mode of the elastic solid, E_{es} the total energy of the elastic solid, and τ_0 the total simulation time, taken as $\tau_0 = 0.8$ ms in all simulations. In each case we plot the proportion of total energy accumulated by N modes.

For weak shock excitation [cf. Fig. 9(a)] the proportion of energy is close to unity even for as low as $N = 3$ modes irrespective of the location of the shock (that is, left or right), and the difference in accumulated energy almost vanishes for $N > 3$, regardless of the model that we adopt. Hence, we observed quick convergence for the accumulated modal en-ergy in this case, with higher-order modes in the plate model being nearly unexcited excited, and with the beam model agreeing well with the plate model. Given the small number of modes required for weak shock excitation we conclude that the elastic solid undergoes low-frequency vibrations in this case, irrespective of the location of application of the shock.

However, a different picture is obtained for moderate and strong shocks [cf. Figs. 9(b) and 9(c)] as the responses of the granular interface exhibit strong nonreciprocity. In these cases, the plate modal energy accumulates much slower when the excitation is applied on the right side, compared to when the same excitation is applied on the left side. For moderate shock applied to the left side the energy on the leading modes dominates the total energy in the elastic solid irrespective if it is modeled as a plate or beam, indicating that the response of the plate model agrees well with that of the beam model; in this case the plate mode undergoes low-frequency vibrations with only a limited number of modes being excited. However, for the moderate shock applied to the right side the plate modal energy converges much more slowly to the total energy, with more energy spread to higher modes, whereas the beam model does not agree well with the plate model. In this case the response of the elastic solid is acoustical rather than vibra-tional, as it involves the excitation of a much higher number of

modes of the elastic solid. Clearly, in this case the beam model fails, as it is incapable of capturing the acoustical response of the elastic solid. These conclusions hold even more for the case of strong shock excitation, where the nonreciprocity of the response subject to left or right shocks is much stronger. Indeed, in Fig. 9(c) the excitation of the higher-order modes of the elastic solid is evident for strong shock applied to the right, and the differences between the beam model and the plate model are significant. However, the accumulated modal energy converges much faster when the strong excitation is applied to the left, compared to when it is applied on the right, a result that highlights even further the nonreciprocal response of the granular interface. Again, in this case we excite vibrations when forcing from the left and acoustics when forcing from the right. These results reveal the strong dependence of nonreciprocity on the energy level of the response, which was to be expected given the strong nonlinearity of the system and demonstrates the passive adaptivity of the response of the nonlinear granular interface on energy (or shock intensity). Even more interesting, the results reported in this work indicate that it is possible to conceive nonreciprocal nonlinear and asymmetric systems that undergo either low-frequency vibrations or high-frequency acoustics depending on the intensity and location of the applied shock excitations.

As mentioned previously, the strong dependence of nonreciprocity on energy originates from the strong nonlinearity of the granular system. With higher impulsive energy, the wave speed in the granular medium is faster both for shock excitations from the left and the right sides, and the corresponding time scales of the acoustical interactions at the interfaces between the LSGM and SSGM and the elastic solid are faster. Moreover, the time scales of the granular-solid interactions are always faster when a shock is applied to the SSGM compared to the LSGM. Therefore, for low impulsive energy, the time scales are relatively slow irrespective of the location of the shock, and only the leading order modes of the elastic solid are excited. For moderate and high impulsive energy, the time scales are much faster and traveling waves are excited in the elastic solid for the case of the SSGM excitation. In this case, the beam model fails to predict the response of the elastic solid. Given the disparity in the sizes of the granules in the SSGM and LSGM, the effects of the higher-order modes are different depending on the location of the shock excitation from due to the different governing time scales of nonlinear primary wavefront scattering (transmission and reflection), and discrete-continuum interfaces, yielding nonreciprocity in the response.

V. CONCLUDING REMARKS

We studied the nonreciprocal acoustics of an 2D initially uncompressed, strongly nonlinear granular-elastic solid interface with asymmetry and internal hierarchy, subject to a half-sine shock excitation applied to either side of the interface. The computational algorithm developed in [29] is adopted and extended here to compute the nonlinear acoustical response of this system, taking into account rotational and frictional effects in the granule responses, and the highly discontinuous nature of the discrete-continuum interactions at the two interfaces of the intermediate elastic solid. The

elastic solid was modeled either as a thin plate in plane stress, or as a much simpler slender beam. The aim of this study was to study the efficacy of the beam model which is mainly valid for low-frequency or wavenumber vibrations, compared to the thin plate model which is valid both for vibrations as well as higher-frequency or wavenumber traveling waves (acoustics).

The break of acoustic reciprocity is studied by examining the responses of the granular media and the intermediate elastic continuum, when the location of the excitation is switched. Due to the strong nonlinearity of the granular media, there occurs a time scale disparity in the propagating wavefronts following the application of the shock when its location is switched. In turn, this yields strong nonreciprocity in the response of the elastic solid, which responds either in the vibration or the acoustics regime. Specifically, when the excitation is applied to a boundary granule of the large-scale granular medium (LSGM) the elastic solid undergoes vibrations with only a few low-frequency or wavenumber modes participating in its response. In this case, the response of the beam model agrees well with the plate model, and the energy of the elastic solid is mainly confined to a few leading-order modes. Moreover, since the time scale of the interaction force between the granules and the solid is relatively slow, the elastic solid is nearly quasistatically excited, and the potential energy overweighs the kinetic energy in this case. However, completely different physics occurs when moderate or strong shock excitations are applied to a boundary granule of the small-scale granular medium (SSGM). In this case, the governing time scales of the interaction forces between the granules and the elastic solid are much faster, and traveling waves propagate within the elastic solid, with its response being in the acoustic regime with many high frequency or wavenumber modes participating. In this case the simpler beam model is not capable of accurately modeling the acoustics of the interface.

Hence, the cause of nonreciprocity in the granular-solid interface can be directly traced to the time scale disparity in the transient response of the intermediate elastic solid either in the vibration or acoustic regime, depending on the location and intensity of the applied shock. In turn, this time scale disparity is due to the strong tunability (with energy) of wave transmission in the component granular media of the interface due to the essentially nonlinear (nonlinearizable) Hertzian contact law governing the granule-to-granule and granule-to-elastic solid interactions. The main features of the acoustics of the elastic solid is then determined by the governing time scales of the granular-elastic solid interactions which are strongly dependent on the excitation levels. In the granular interface considered, traveling waves (acoustics) in the elastic solid occur for moderate and strong shocks applied to the SSGM, whereas vibrations in the elastic solid occur for weak excitations or when the excitations are applied to the LSGM.

Hence, the presented granular-solid interface is a new paradigm of a completely passive (hybrid) discrete-continuum system, which, depending on the location and intensity of the shock excitation exhibits completely different nonreciprocal response regimes: (1) acoustics in the granular media and vibrations in the elastic continuum or (2) acoustics in both the

granular media and the elastic continuum. To our knowledge, such a tunability of the response to either vibrations and/or acoustics depending on the type and location of the excitation, is presented for the first time for a passive mechanical system. It is clear that what enables the coexistence of dynamics and acoustics in the interface is the break of classical reciprocity through the synergy of asymmetry (different-scale granular media on the right and left) and strong nonlinearity (of the granular media).

The reported nonreciprocal acoustics of the considered 2D granular-elastic solid interface may guide the designs of new types of efficient granular mitigators or granular-based "acoustic diodes" supporting unidirectional (preferred) wave transmission in specific energy and frequency ranges. It would be of interest to extend of the interface to narrowband loads (e.g., harmonic excitations), in order to study the tunability of the response and the break of acoustic reciprocity subject to this type of excitations as well. In addition, it would be of interest to study if the coexistence of vibrations and waves could be achieved for narrowband loads as well. In a more general context, the passive tunability of acoustic nonreciprocity to energy could be exploited when designing nonlinear interfaces with performance tailored to the frequency or wavenumber and energy contents of the applied broadband or narrowband excitations. This could also find applications to new types of vibration energy harvesters whose operation would be based on the nonreciprocal features of such interfaces.

APPENDIX A: BRIEF DETAILS OF THE COMPUTATIONAL ALGORITHM [27]

Referring to the governing equations of the granular media (1) and the elastic solid (8), these are coupled through the interaction force vector $\boldsymbol{F}$. Given the solution of the system at the time instant $\tau = \tau_s$, the iteration-interpolation algorithm calculating the interaction forces at the next time step $\tau = \tau_{s+1}$ can be summarized in the following steps:

Step 1: We start with an initial guess for the interaction force vector $\boldsymbol{F}_{s+1}^{(1)} = \boldsymbol{F}_s^C$, where the subscript $(s+1)$ refers to evaluation at time instant τ_{s+1}, the superscript (1) denotes the first iteration, and $\boldsymbol{F}_s^C$ denotes the converged force vector at the previous time instant τ_s (for the initial time instant $\tau_0 = 0$ we consider the trivial initial guess, $\boldsymbol{F}_0^C = 0$).

Step 2: Based on the initial guess of $\boldsymbol{F}_{s+1}^{(1)}$, we compute the response of the elastic solid at the time instant τ_{s+1} based on the β-Newmark method. To this end, the governing equation of motion are expressed as

$$\dot{\boldsymbol{x}}_{s+1}^{(1)} = \dot{\boldsymbol{x}}_s^C + \left[(1-\gamma)\ddot{\boldsymbol{x}}_s^C + \gamma\ddot{\boldsymbol{x}}_{s+1}^{(1)} \right] \Delta\tau,$$

$$\boldsymbol{x}_{s+1}^{(1)} = \boldsymbol{x}_s^C + \dot{\boldsymbol{x}}_s^C \Delta\tau + \left[\frac{1-2\beta}{2}\ddot{\boldsymbol{x}}_s^C + \beta\ddot{\boldsymbol{x}}_{s+1}^{(1)} \right] \Delta\tau^2$$

$$\boldsymbol{M}\ddot{\boldsymbol{x}}_{s+1}^{(1)} + \boldsymbol{K}\boldsymbol{x}_{s+1}^{(1)} = \boldsymbol{F}_{s+1}^{(1)}, \tag{A1}$$

where $\boldsymbol{x}_{s+1}^{(1)}$ denotes the first iteration of the displacement vector $\boldsymbol{x}$ at the time instant τ_{s+1}, $\boldsymbol{x}_s^C$ denotes the converged value of the displacement vector $\boldsymbol{x}$ at the previous time instant τ_s, and $\beta = 1/4$ and $\gamma = 1/2$ are the two coefficients of the β-Newmark method, yielding the constant averaged acceleration variant. The solutions of Eqs. (A1) are given by

$$\ddot{\boldsymbol{x}}_{s+1}^{(1)} = \left(\boldsymbol{M} + \frac{1}{4}\boldsymbol{K}\Delta\tau^2 \right)^{-1}$$
$$\times \left[\boldsymbol{F}_{s+1}^{(1)} - \boldsymbol{K}\left(\boldsymbol{x}_s^C + \dot{\boldsymbol{x}}_s^C \Delta\tau + \frac{1}{4}\ddot{\boldsymbol{x}}_s^C \Delta\tau^2 \right) \right],$$

$$\dot{\boldsymbol{x}}_{s+1}^{(1)} = \dot{\boldsymbol{x}}_s^C + \frac{\ddot{\boldsymbol{x}}_s^C + \ddot{\boldsymbol{x}}_{s+1}^{(1)}}{2}\Delta\tau,$$

$$\boldsymbol{x}_{s+1}^{(1)} = \boldsymbol{x}_s^C + \dot{\boldsymbol{x}}_s^C \Delta\tau + \frac{1}{2}\left(\frac{\ddot{\boldsymbol{x}}_s^C + \ddot{\boldsymbol{x}}_{s+1}^{(1)}}{2} \right)\Delta\tau^2, \tag{A2}$$

where $\Delta\tau = \tau_{s+1} - \tau_s$ denotes the time step between successive time instants.

Step 3: Interpolate the response of the elastic solid with constant averaged acceleration $(\ddot{\boldsymbol{x}}_s^C + \ddot{\boldsymbol{x}}_{s+1}^{(1)})/2$. The response between time instants τ_s and τ_{s+1} is given by

$$\dot{\boldsymbol{x}}^{(1)}(\tau) = \dot{\boldsymbol{x}}_s^C + \frac{\ddot{\boldsymbol{x}}_s^C + \ddot{\boldsymbol{x}}_{s+1}^{(1)}}{2}(\tau - \tau_s),$$

$$\boldsymbol{x}^{(1)}(\tau) = \boldsymbol{x}_s^C + \dot{\boldsymbol{x}}_s^C(\tau - \tau_s) + \frac{1}{2}\left(\frac{\ddot{\boldsymbol{x}}_s^C + \ddot{\boldsymbol{x}}_{s+1}^{(1)}}{2} \right)(\tau - \tau_s)^2. \tag{A3}$$

Step 4: Given the response of the elastic solid, $\boldsymbol{x}_{s+1}^{(1)}(\tau)$, the response of the flexible boundary $\boldsymbol{u}_{ki}^{(1)}$ at contact point k of the elastic solid is determined. Therefore, the DE equations of the granular medium (1) subject to the constitutive relations (5) and (6) and the boundary conditions $\boldsymbol{u}_{ki} = \boldsymbol{u}_{ki}^{(1)}$ can be solved using the fourth-order Runge-Kutta method. This provides the first iteration for the responses of the granular media.

Step 5: Compute the interaction forces through the relations (5) and (6) based on the first iteration of the granular responses and the boundary responses $\boldsymbol{u}_{ki}^{(1)}$ of the elastic solid Assemble the external force vector applied to the elastic solid medium with the interaction forces being computed based on the second iteration of the force vector, $\boldsymbol{F}_{s+1}^{(2)}$.

Step 6: Repeat steps 1–5 until the interaction force vector converges. The convergence condition is given by

$$\left| F_{(s+1),n}^{(j+1)} - F_{(s+1),n}^{(j)} \right| < \text{Abstol}, \quad \frac{\left| F_{(s+1),n}^{(j+1)} - F_{(s+1),n}^{(j)} \right|}{\left| F_{(s+1),n}^{(j)} \right|}$$
$$< \text{Reltol}, \tag{A4}$$

where $F_{(s+1),n}^{(j)}$ denotes the nth element of the jth iteration of the interaction force vector $\boldsymbol{F}$ at the time instant τ_{s+1}, and Abstol and Reltol preset absolute and relative tolerances, respectively. The force vector $\boldsymbol{F}_{s+1}$ is assumed to be converged as long as $(A-4)$ is satisfied for all of its nonzero elements.

Step 7: Once the interaction forces at the time instant τ_{s+1} has converged, and the force vector $\boldsymbol{F}_{s+1} = \boldsymbol{F}_{s+1}^C$ is computed, the converged response of the elastic solid at time instant

τ_{s+1} is computed by (A2) and the converged responses of the granular media at the same time instant are computed by the Runge-Kutta method. Then we repeat steps 1–6 in order to get the responses at the time next instants $\tau_{s+2}, \tau_{s+3}, \dots$ until the simulation time is completed.

As a result of steps 1–5 a nonlinear map $\boldsymbol{F}_{s+1} \to \boldsymbol{F}_{s+1}$ is constructed. The stability of this map is crucial for the numerical convergence of the computational algorithm and needs to be carefully considered, since this ensures that the iteration in step 6 converges to the fixed point of the map. To this end, we assume that there are N nonzero elements in $\boldsymbol{F}_{s+1}$, then the previous vector map yields an N-dimensional nonlinear map. The stability condition for the iteration is all moduli of the N eigenvalues are smaller than unity. A special consideration is given to the plate model for large k_s values, which is a parameter in the Coulomb-tanh friction force (5), i.e., when the friction forces at the boundaries are sensitive to the relative tangential velocity. At this point we note that the Jacobian matrix of the N-dimensional nonlinear map is given by

$$\frac{\partial \boldsymbol{F}_{s+1}^{(j+1)}}{\partial \boldsymbol{F}_{s+1}^{(j)}} = \frac{\partial \boldsymbol{F}_{s+1}^{(j+1)}}{\partial \left(\boldsymbol{x}_{s+1}^{(j)}, \dot{\boldsymbol{x}}_{s+1}^{(j)} \right)} \frac{\partial \left(\boldsymbol{x}_{s+1}^{(j)}, \dot{\boldsymbol{x}}_{s+1}^{(j)} \right)}{\partial \boldsymbol{F}_{s+1}^{(j)}}. \qquad \text{(A5)}$$

Notice that the term $\frac{\partial (\boldsymbol{x}_{s+1}^{(j)}, \dot{\boldsymbol{x}}_{s+1}^{(j)})}{\partial \boldsymbol{F}_{s+1}^{(j)}}$ is solely determined by the FE equations of the elastic solid, and the term $\frac{\partial \boldsymbol{F}_{s+1}^{(j+1)}}{\partial (\boldsymbol{x}_{s+1}^{(j)}, \dot{\boldsymbol{x}}_{s+1}^{(j)})}$ by the DE granular equations. Hence, for large values of k_s, a small variation in the boundary condition $\boldsymbol{u}_{ki}^{(j)}$ yields a large variation in the corresponding interaction forces. In the limit of the Coulomb frictional model when $k_s \to +\infty$, the term $\frac{\partial \boldsymbol{F}_{s+1}^{(j+1)}}{\partial (\boldsymbol{x}_{s+1}^{(j)}, \dot{\boldsymbol{x}}_{s+1}^{(j)})}$ becomes unbounded and the computational algorithm cannot converge and becomes numerically unstable.

In the following analysis we provide a brief discussion of the numerical stability of the computational response of the thin plate model which involves friction forces (no such forces are involved in the slender beam model), and for a more detailed analysis we refer to [29]. To start with, we introduce several assumptions to simplify the previous expressions.

Assumption 1: Since the time step $\Delta \tau$ is small, we assume that the variation of the interaction forces at time instant τ_{s+1} has only a local effect on the response of the plate. That is, the variations of the interaction forces at a contact point between the plate and the granular medium at τ_{s+1} has negligible effects on the responses of the plate at the other contact points at the same time step τ_{s+1}.

Assumption 2: Since the effects of the interaction forces are assumed to be local and the interaction forces are applied at the middle points of the small rigid layers [cf. Figs. 2(c) and 2(d)], the normal and tangential responses of the rigid layers are decoupled due to symmetry. That is, normal interaction forces do not yield tangential responses of the rigid layers, and tangential interaction forces do not generate normal responses.

Assumption 3: Given the great disparity in mass between a single contacting granule and the finite elements of the plate attached to the contacting rigid layer, the response of the rigid layer is much more sensitive to changes in the interaction forces compared to the response of the contacting granule.

Therefore, we neglect the sensitivities related to the granule responses.

Based on these three assumptions, the nonlinear ND *global* map $\boldsymbol{F}_{s+1} \to \boldsymbol{F}_{s+1}$ is simplified as N decoupled nonlinear 1D *local* maps since the variation of each element of $\boldsymbol{F}_{s+1}$ does not affect the other elements. We pay special attention to the local maps related to friction forces. The linearized eigenvalue $\lambda_{ki,t,(s+1)}$ of the local map of the friction interaction force between the kth contact point of the plate and the ith granule can be evaluated as

$$\lambda_{ki,t,(s+1)} = \frac{\partial f_{ki,(s+1)}^{(j+1)}}{\partial f_{ki,(s+1)}^{(j)}} = \frac{\partial f_{ki,(s+1)}^{(j+1)}}{\partial \dot{x}_{ki,(s+1)}^{(j)}} \frac{\partial \dot{x}_{ki,(s+1)}^{(j)}}{\partial f_{ki,(s+1)}^{(j)}}, \qquad \text{(A6)}$$

where $f_{ki,(s+1)}^{(j+1)}$ denotes the $(j+1)$th iteration of the tangential interaction force applied from the ith granule to the kth contact point of the plate at time instant τ_{s+1}, and $\dot{x}_{ki,(s+1)}^{(j)}$ denotes the relative tangential velocity between the kth contact point of the plate and the ith granule at time instant τ_{s+1}. The positive direction of $f_{ki,(s+1)}^{(j+1)}$ and $\dot{x}_{ki,(s+1)}^{(j)}$ agrees with the positive direction of the tangential degree of freedom of the rigid layer at the contact point. Based on the constitutive relation (5) of the DE granular equations and with the sensitivity of granule response neglected, the first term $\frac{\partial f_{ki,(s+1)}^{(j+1)}}{\partial \dot{x}_{ki,(s+1)}^{(j)}}$ is approximated by

$$\left| \frac{\partial f_{ki,(s+1)}^{(j+1)}}{\partial \dot{x}_{ki,(s+1)}^{(j)}} \right| = \mu k_s \left| \boldsymbol{N}_{ik,(s+1)}^{(j+1)} \right| \cosh^{-2} \left(k_s \dot{\delta}_{t,ik,(s+1)}^{(j+1)} \right), \qquad \text{(A7)}$$

where the sign is dependent on whether the unit vector $\boldsymbol{t}_{ik}$ defined in the DE equations agrees with the direction of the tangential driving DOF of the rigid layer in the FE model. The second term $\frac{\partial \dot{x}_{ki,(s+1)}^{(j)}}{\partial f_{ki,(s+1)}^{(j)}}$ is determined by the FE equations, which can be explicitly expressed from (A2) after some algebraic manipulations as

$$\frac{\partial \dot{x}_{ki,(s+1)}^{(j)}}{\partial f_{ki,(s+1)}^{(j)}} = \frac{1}{2} \Delta \tau \, \boldsymbol{T}_{i,t} \left(\boldsymbol{M} + \frac{1}{4} \boldsymbol{K} \Delta \tau^2 \right)^{-1} \boldsymbol{T}_{i,t}{}^T, \qquad \text{(A8)}$$

where $\boldsymbol{T}_{i,t}$ is a sparse vector such that $\dot{x}_{ki,(s+1)}^{(j)} = \boldsymbol{T}_{i,t} \dot{\boldsymbol{x}}_{s+1}^{(j)}$. The only nonzero element of $\boldsymbol{T}_{i,t}$ with value equal to unity is located on the tangential driving DOF of the rigid layer at the kth contact point between the ith granule and the boundary of the plate. The modulus of the eigenvalue associated with the frictional interaction force is computed based on (A7) and (A8). For convenience we replace the variables at the time instant τ_{s+1} with the variables at the time instant τ_s, so that the modulus of the eigenvalue is approximated as

$$|\lambda_{ki,t,(s+1)}| = \frac{1}{2} \mu k_s \left| N_{ik,s}^C \right| \Delta \tau \, \boldsymbol{T}_{i,t} \left(\boldsymbol{M} + \frac{1}{4} \boldsymbol{K} \Delta \tau^2 \right)^{-1} \boldsymbol{T}_{i,t}{}^T$$
$$\times \cosh^{-2} \left(k_s \dot{\delta}_{t,ik,s}^C \right). \qquad \text{(A9)}$$

It can be shown that all eigenvalues of the local nonlinear maps associated with the normal interaction forces are unconditionally stable, so they do not need to be considered in the stability analysis [27]. The eigenvalues corresponding
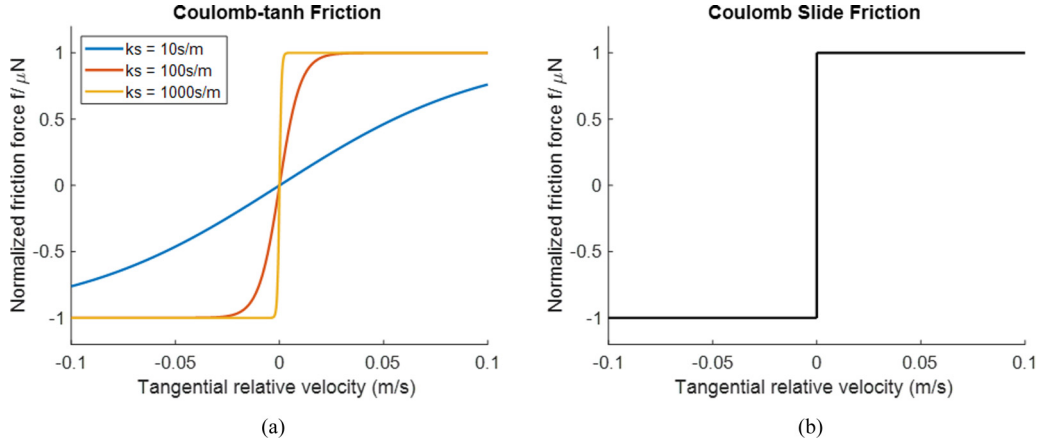
FIG. 10. Force-velocity constitutive relation of (a) the smooth Coulomb-tanh friction model and (b) the discontinuous Coulomb dry friction model.

to all k contact points between the plate and the LSGM and SSGM can be evaluated by (A9) and need to be evaluated at each time instant and for every contact point; otherwise the simplified local map diverges and the interaction force at the current time instant diverges leading to numerical instability

APPENDIX B: DETAILS OF THE SELF-ADAPTIVE PROCESS AND A NUMERICAL EXAMPLE

In Fig. 10 we depict the tanh-Coulomb friction model used in this study and compare it to the discontinuous Coulomb dry friction model. As discussed in the paper, the latter one is unconditionally unstable, i.e., it yields linearized eigenvalues (A9) that exceed unity in certain time steps, which prevents numerical convergence of the computational algorithm. On the contrary, the smooth tanh-Coulomb model enables adaptive selection of the time step of the numerical simulation that ensures numerical stability of the algorithm. This is described below by means of a numerical example

to show the details of the numerical simulation as well as the way that we check of moduli of the eigenvalues (A9). In all simulations the initial time step is selected as $\Delta \tau_0 = 4 \times 10^{-8}$ s, and set as constant when using the beam model for the elastic solid. When the plate model is adopted, the eigenvalue moduli (A9) are checked at each time instant. Due to the symmetry of the acoustics, only the eigenvalues corresponding to frictional interactions between granules 10, 11, and 12 of the LSGM [cf. Fig. 10(b)] and the left edge of the plate are labelled as λ_{10}, λ_{11}, and λ_{12}, respectively, and are checked to satisfy the stability condition (10). Similarly, the eigenvalues corresponding to the frictional interactions between the granules J, K, and L of the SSGM and right edge of the plate are checked and named labelled as λ_J, λ_K, and λ_L, respectively.

The eigenvalues at these six contact points are available by plugging the initial time step increment $\Delta \tau = \Delta \tau_0 = 4 \times 10^{-8}$ s into (10). As one of the six eigenvalues is greater than 0.5, a smaller time step $\Delta \tau = \Delta \tau_1 = \frac{1}{2} \Delta \tau_0$ is adopted. Note that the eigenvalues being proportional to the increment
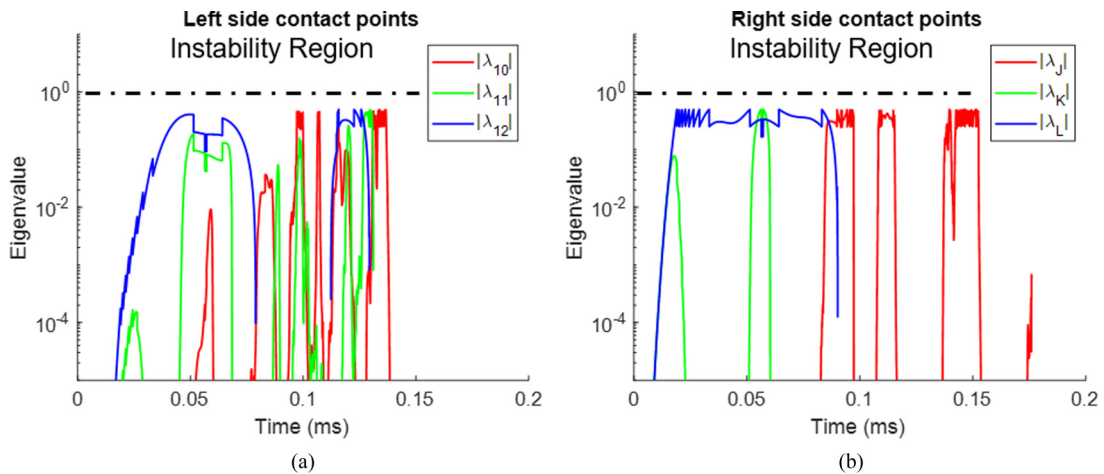

FIG. 11. Moduli of the six eigenvalues for strong shock applied to the granule C of the SSGM, at the three contact points (a) on the left boundary of the plate and (b) on the right boundary of the plate; note the discontinuous nature of the eigenvalues due to the adaptive change of the time step.

in the time steps, become smaller as the time step is decreased. The general rule for adaptively selecting the time step increment $\Delta \tau_n$ is by satisfying the following two criteria:

$$\Delta \tau = \Delta \tau_0, \ \max \left(\lambda(\Delta \tau_0) \right) \leqslant \frac{1}{2},$$

$$\Delta \tau = \Delta \tau_n = \frac{\Delta \tau_0}{2^n},$$

$$\frac{1}{4} < \max \left(\lambda(\Delta \tau_n) \right) = \frac{\max \left(\lambda(\Delta \tau_0) \right)}{2^n} \leqslant \frac{1}{2}. \qquad \text{(B1)}$$

That is, the initial time step $\Delta \tau_0$ is divided by a sufficiently large integer power of 2 so that the corresponding moduli of all eigenvalues are smaller or equal than $\frac{1}{2}$; this ensures that the iteration converges fast to the fixed point of the nonlinear map and the algorithm converges quickly to the solution of the given time step.

To check the validity of our algorithm, we pick the case for strong shock applied to granule C of the SSGM; cf. Figs. 4(f), 6(c), 7(b), and 8(b). This corresponds to the most critical case since the corresponding iteration is the more challenging from a convergence point of view. From Figs 7(b) and 8(b) we note that the primary wavefront reaches the intermediate plate and starts getting scattered at around ~ 0.02 ms. The corresponding moduli of the six eigenvalues are plotted in Fig. 11 for $\tau = 0$–0.2 ms, and are all smaller

than unity, which ensures the convergence of the simulation. Note that the eigenvalues are not smooth due to the necessary (adaptive) change in the time step increment $\Delta \tau$ during successive time steps to ensure convergence as discussed previously.

APPENDIX C: ANIMATIONS OF THE ENERGY DISTRIBUTIONS

Here we provide the animations that better visualize the nonlinear acoustics of the granular-elastic solid interface for weak, moderate, and strong shock excitations (these correspond to the results presented in the main text) in the Supplemental Material [49]. The animations are grouped into two main categories: (1) videos of deformations and (2) animations of instantaneous normalized energy densities. For better visualization, the magnification factor for the animations of the deformations are $\times 5000$ for weak, $\times 1000$ for moderate, and $\times 200$ for strong shock excitation. At each shock level we consider the excitation of either granule 3 of the LSGM of granule C of the SSGM.

The animations are also available through the following links: links for animations of the deformations [50] and links for animations of the normalized energy densities [51] .

[1] A. Lazaridi and V. Nesterenko, Observation of a new type of solitary waves in a one-dimensional granular medium, J. Appl. Mech. Tech. Phys. **26**, 405 (1985).

[2] V. Nesterenko, Propagation of nonlinear compression pulses in granular media, J. Appl. Mech. Tech. Phys. **24**, 733 (1983).

[3] V. Nesterenko, Solitary waves in discrete media with anomalous compressibility and similar to sonic vacuum, in *EURODYMAT 1994–4th International Conference on Mechanical and Physical Behaviour of Materials under Dynamic Loading*, Oxford, 1994.

[4] V. Nesterenko, *Dynamics of Heterogeneous Materials* (Springer-Verlag, New York, 2001).

[5] C. Daraio, V. Nesterenko, E. Herbold, and S. Jin, Strongly nonlinear waves in a chain of Teflon beads, Phys. Rev. E **72**, 016603 (2005).

[6] M. Hasan, S. Cho, K. Remick, A. Vakakis, D. McFarland, and W. Kriven, Experimental study of nonlinear acoustic bands and propagating breathers in ordered granular media embedded in matrix, Granular Matter **17**, 49 (2015).

[7] Y. Starosvetsky and A. Vakakis, Traveling waves and localized modes in one-dimensional homogeneous granular chains with no precompression, Phys. Rev. E **82**, 026603 (2010).

[8] Y. Starosvetsky, M. Hasan, A. Vakakis, and L. Manevitch, Strongly nonlinear beat phenomena and energy exchanges in weakly coupled granular chains on elastic foundations, SIAM J. Appl. Math. **72**, 337 (2012).

[9] Z. Zhang, L. Manevitch, V. Smirnov, L. Bergman, and A. Vakakis, Extreme nonlinear energy exchanges in a geometrically nonlinear lattice oscillating in the plane, J. Mech. Phys. Solids **110**, 1 (2018).

[10] M. Hasan, Y. Starosvetsky, A. Vakakis, and L. Manevitch, Nonlinear targeted energy transfer and macroscopic analog of

the quantum Landau–Zener effect in coupled granular chains, Physica D **252**, 46 (2013).

[11] Z. Zhang, I. Koroleva, L. Manevitch, L. Bergman, and A. Vakakis, Nonreciprocal acoustics and dynamics in the in-plane oscillations of a geometrically nonlinear lattice, Phys. Rev. E **94**, 032214 (2016).

[12] Q. Zhang, W. Li, J. Lambros, L. A. Bergman, and A. F. Vakakis, Pulse transmission and acoustic non-reciprocity in a granular channel with symmetry-breaking clearances, Granular Matter **22**, 20 (2020).

[13] J. Cui, T. Yang, and L. Chen, Frequency-preserved non-reciprocal acoustic propagation in a granular chain, Appl. Phys. Lett. **112**, 181904 (2018).

[14] A. Spadoni and C. Daraio, Generation and control of sound bullets with a nonlinear acoustic lens, Proc. Natl. Acad. Sci. USA **107**, 7230 (2010).

[15] C. Donahue, P. Anzel, L. Bonanomi, T. Keller, and C. Daraio, Experimental realization of a nonlinear acoustic lens with a tunable focus, Appl. Phys. Lett. **104**, 014103 (2014).

[16] F. Melo, S. Job, F. Santibanez, and F. Tapia, Experimental evidence of shock mitigation in a Hertzian tapered chain, Phys. Rev. E **73**, 041305 (2006).

[17] J. Hong, Universal Power-Law Decay of the Impulse Energy in Granular Protectors, Phys. Rev. Lett. **94**, 108001 (2005).

[18] S. Sen, F. Manciu, and M. Manciu, Thermalizing an impulse, Physica A **299**, 551 (2001).

[19] B. Lawney and S. Luding, Frequency filtering in disordered granular chains, Acta Mech. **225**, 2385 (2014).

[20] F. Li, P. Anzel, J. Yang, P. G. Kevrekidis, and C. Daraio, Granular acoustic switches and logic elements, Nat. Commun. **5**, 5311 (2014).

[21] G. Yang, B. Zhang, P. Lv, and Q. Zhou, Behaviour of geogrid re-inforced soil retaining wall with concrete-rigid facing, Geotext. Geomembr. **27**, 350 (2009).

[22] L. Wang, G. Chen, and S. Chen, Experimental study on seismic response of geogrid reinforced rigid retaining walls with saturated backfill sand, Geotext. Geomembr. **43**, 35 (2015).

[23] R. Potekin, D. M. McFarland, and A. F. Vakakis, Nonlinear wave scattering at the flexible interface of a granular dimer chain, Granular Matter **18**, 68 (2016).

[24] Q. Zhang, R. Potekin, W. Li, and A. Vakakis, Nonlinear wave scattering at the interface of granular dimer chains and an elastically supported membrane, Int. J. Solids Struct. **182**, 46 (2020).

[25] J. Yang and M. Sutton, Nonlinear wave propagation in a hexagonally packed granular channel under rotational dynamics, Int. J. Solids Struct. **77**, 65 (2015).

[26] C. Goldenberg and I. Goldhirsch, Friction enhances elasticity in granular solids, Nature (London) **435**, 188 (2005).

[27] J. Chattoraj, O. Gendelman, M. Ciamarra, and I. Procaccia, Oscillatory Instabilities in Frictional Granular Matter, Phys. Rev. Lett. **123**, 098003 (2019).

[28] H. Charan, O. Gendelman, I. Procaccia, and Y. Sheffer, Giant amplification of small perturbations in frictional amorphous solids, Phys. Rev. E **101**, 062902 (2020).

[29] C. Wang, Q. Zhang, and A. F. Vakakis, Wave transmission in 2D nonlinear granular-solid interfaces, including rotational and frictional effects, Granular Matter **23**, 21 (2021).

[30] J. Achenbach, *Reciprocity in Elastodynamics* (Cambridge University Press, Cambridge, 2009).

[31] K. Tsakmakidis, L. Shen, S. Schulz, X. Zheng, J. Upham, X. Deng, H. Altug, A. Vakakis, and R. W. Boyd, Breaking Lorentz reciprocity to overcome the time-bandwidth limit in physics and engineering, Science **356**, 1260 (2017).

[32] R. Fleury, D. Sounas, C. Sieck, M. Haberman, and A. Alù, Sound isolation and giant linear nonreciprocity in a compact acoustic circulator, Science **343**, 516 (2014).

[33] S. Cummer, Selecting the direction of sound transmission, Science **343**, 495 (2014).

[34] R. Fleury, D. Sounas, and A. Alù, Subwavelength ultrasonic circulator based on spatiotemporal modulation, Phys. Rev. B **91**, 174306 (2015).

[35] J. Bunyan, K. Moore, A. Mojahed, M. Fronk, M. Leamy, S. Tawfick, and A. Vakakis, Acoustic nonreciprocity in a lattice incorporating nonlinearity, asymmetry, and internal scale hierarchy: Experimental study, Phys. Rev. E **97**, 052211 (2018).

[36] K. Moore, J. Bunyan, S. Tawfick, O. Gendelman, S. Li, M. Leamy, and A. Vakakis, Nonreciprocity in the dynamics of

coupled oscillators with nonlinearity, asymmetry, and scale hierarchy, Phys. Rev. E **97**, 012219 (2018).

[37] M. Fronk, S. Tawfick, C. Daraio, S. Li, A. Vakakis, and M. Leamy, Acoustic non-reciprocity in lattices with nonlinearity, internal hierarchy, and asymmetry: Computational study, J. Vib. Acoust. **141**, 051011 (2019).

[38] Y. Starosvetsky, K. Jayaprakash, M. Hasan, and A. Vakakis, *Topics on the Nonlinear Dynamics and Acoustics of Ordered Granular Media* (World Scientific, Singapore, 2017).

[39] Y. Tsuji, T. Tanaka, and T. Ishida, Lagrangian numerical simulation of plug flow of cohesionless particles in a horizontal pipe, Powder Technol. **71**, 239 (1992).

[40] P. Cundall and O. Strack, A discrete numerical model for granular assemblies, Geotechnique **29**, 47 (1979).

[41] Y. Starosvetsky and A. Vakakis, Primary wave transmission in systems of elastic rods with granular interfaces, Wave Motion **48**, 568 (2011).

[42] S. Andersson, A. Söderberg, and S. Björklund, Friction models for sliding dry, boundary and mixed lubricated contacts, Tribol. Int. **40**, 580 (2007).

[43] E. Pennestrì, V. Rossi, P. Salvini, and P. Valentini, Review and comparison of dry friction force models, Nonlinear Dyn. **83**, 1785 (2016).

[44] S. Timoshenko and J. Goyder, *Theory of Elasticity*, 3rd ed. (McGraw-Hill, New York, 2010).

[45] V. Nesterenko, C. Daraio, E. Herbold, and S. Jin, Anomalous Wave Reflection at the Interface of Two Strongly Nonlinear Granular Media, Phys. Rev. Lett. **95**, 158702 (2005).

[46] A. Tichler, L. Gomez, N. Upadhyaya, X. Campman, V. Nesterenko, and V. Vitelli, Transmission and Reflection of Strongly Nonlinear Solitary Waves at Granular Interfaces, Phys. Rev. Lett. **111**, 048001 (2013).

[47] M. Hasan, A. Vakakis, and D. McFarland, Nonlinear localization, passive wave arrest and traveling breathers in two-dimensional granular networks with discontinuous lateral boundary conditions, Wave Motion **60**, 196 (2016).

[48] A. Vakakis, L. Manevitch, Y. Mikhlin, V. Pilipchuk, and A. Zevin, *Normal Modes and Localization in Nonlinear Systems* (John Wiley & Sons, New York, 1996).

[49] See Supplemental Material at http://link.aps.org/supplemental/10.1103/PhysRevE.104.044906 for animations of the motions and the energy density with the excitation applied on the LSGM and SSGM for weak, moderate and strong excitations respectively.

[50] https://uofi.box.com/s/qpgt6mz691c7k35mz0ej297e90qrjtrd.

[51] https://uofi.box.com/s/zx3mmmsnnitfjfzxqsjrufgaemc0o9zx.